UCRL-BOOK-402632

07

mst

publications and patents

materials science and technology division

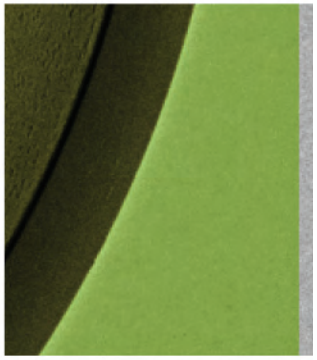

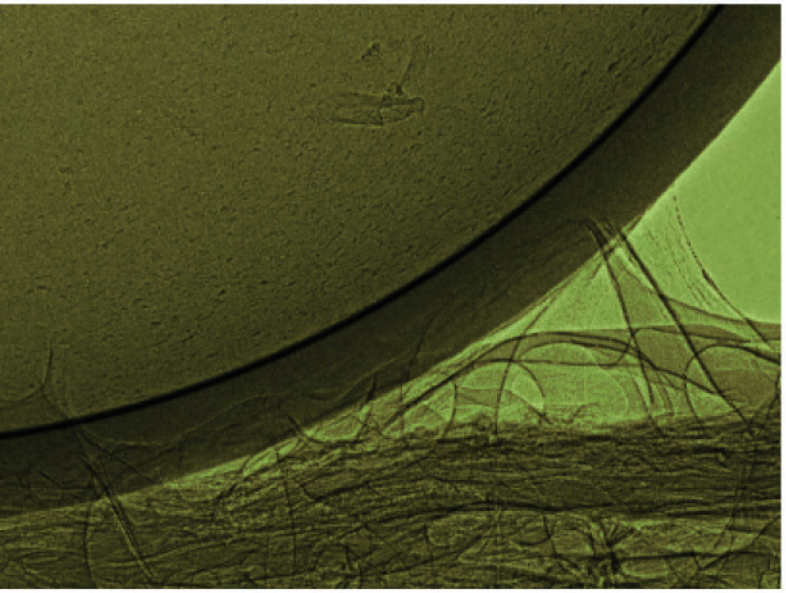

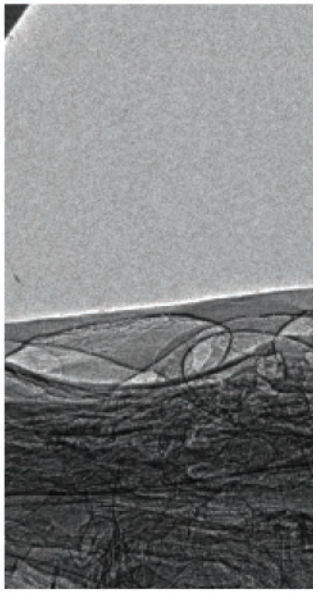

chemistry, materials, earth and life sciences directorate

lawrence livermore national laboratory

About the cover ...

Radiograph of a 2 mm diameter diamond capsule intended for for inertial confinement fusion (ICF) experiments at the National Ignition Facility (NIF). The diamond capsule has a thickness of approximately 80 microns, and is polished to a root mean square surface finish of better than 10 nm. Diamond has very attractive material properties for the ICF application including the highest atomic density of any known material, a low atomic number, and a high yield strength. The fabrication of these hollow, ultra-high precision diamond shells is extremely challenging, and was made possible by a successful collaboration of researchers from the Nanoscale Synthesis and Characterization Laboratory (NSCL) of LLNL, and the Fraunhofer Institute of Applied Solid State Physics in Germany. The radiograph was acquired by Nick E. Teslich.

Lawrence Livermore National Laboratory is operated by Lawrence Livermore National Security, LLC, for the U.S. Department of Energy, National Nuclear Security Administration under Contract DE-AC52-07NA27344.

April 2008

UCRL-BOOK-402632
By W. E. King

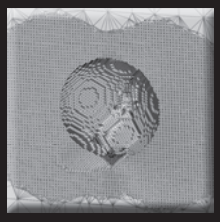

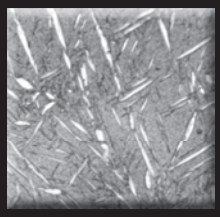

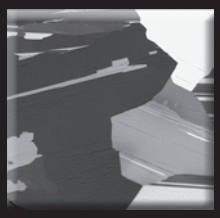

Materials Science & Technology Division

The Materials Science and Technology Division (MSTD) supports the central scientific and technological missions of the Laboratory, and at the same time, executes world-class, fundamental research and novel technological development over a wide range of disciplines. Our organization is driven by the institutional needs in nuclear weapons stockpile science, high-energy-density science, nuclear reactor science, and energy and environment science and technology. We maintain expertise and capabilities in many diverse areas, including actinide science, electron microscopy, laser-materials interactions, materials theory, simulation and modeling, materials synthesis and processing, materials science under extreme conditions, ultrafast materials science, metallurgy, nanoscience and technology, nuclear fuels and energy security, optical materials science, and surface science. MSTD scientists play leadership roles in the scientific community in these key and emerging areas.

Solving Problems of National Importance

Our division is well-aligned with missions in the U.S. Stockpile Stewardship Program, the National Ignition Facility (NIF), Energy and Environment, and the nation's counterproliferation and security efforts. We deliver high value to the nation through excellence in science as well as use of large-scale DOE facilities and resources in experiment and simulation.

Materials Science for Stockpile Stewardship: A major element of our program involves the study of materials behavior over a wide range of timescales, pressures and temperatures. We employ multiple approaches, including time-resolved observations, recovery-based studies, and large-scale computational modeling, to better understand how factors such as aging or extreme dynamic stress affect phase, strength, and damage evolution in materials.

Materials Science at the Largest Laser in the World: Central to the use of NIF lasers at the highest energy thresholds has been our ongoing contributions in the production of laser materials as well as the understanding of laser materials interactions. MSTD scientists play a key role in examining the fundamental processes that initiate laser damage. We also

lead the development of next-generation target fabrication, an effort that is heavily leveraged on our metallurgical and nanoscience competencies. In partnership with NIF, we are developing future diagnostics, such as time-resolved x-ray based diffraction and scattering.

Groundbreaking Science

The predictive understanding of properties and performance of materials over a broad range of conditions is at the frontier of materials science. MSTD is addressing fundamental problems of national importance through diverse experimental and theoretical capabilities.

Ultrafast Dynamics of Materials: Understanding the dynamic response of solids under extreme pressures, temperatures, and strain rates remains an exciting scientific frontier in materials science. Our scientists can directly probe phase transformations that result from dynamic changes, through combined approaches that include ultrafast x-ray probes, dynamic transmission electron microscopy, and large-scale molecular dynamics simulations.

Nanoscience and Technology: Through the use of advanced synthesis and fabrication techniques along with atomic-scale characterization, we are developing nanoscale materials to address vital national security needs. High-resolution studies coupled with state-of-the-art simulations are being used to predictively understand the properties and performance of these materials. These tailored materials will potentially find revolutionary applications in areas that include novel catalysts, photonic crystals, and advanced membranes.

Materials Simulations: Scientists in MSTD are able to simulate the behavior of materials from the atomic to the microstructural scale. At the atomic scale researchers are using the world's fastest computers to investigate material behavior under extreme conditions. At the microstructural level, modeling of dislocation movement has uncovered novel mechanisms for dislocation motion and interaction.

MSTD Management

Wayne E. King, Division Leader
Hector E. Lorenzana, Deputy Division Leader for Science and Technology
Tammy S. Gdowski, Deputy Division Leader for Operations
Sherene M. Goulart-Shankel, Division Administrator

Publications

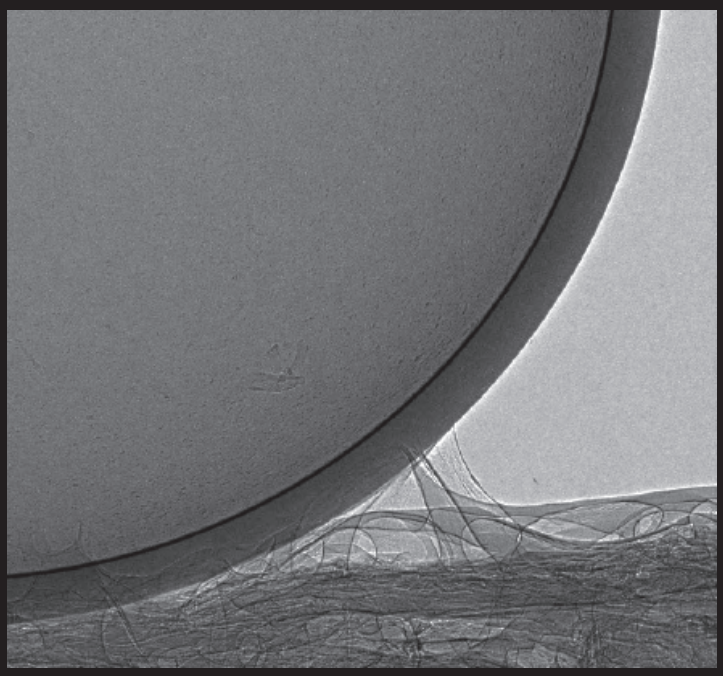

2007

Ultrafast bond softening in bismuth: Mapping a solid's interatomic potential with X-rays

Fritz, D. M., D. A. Reis, B. Adams, R. A. Akre, J. Arthur, C. Blome, P. H. Bucksbaum, A. L. Cavalieri, S. Engemann, S. Fahy, R. W. Falcone, P. H. Fuoss, K. J. Gaffney, M. J. George, J. Hajdu, M. P. Hertlein, P. B. Hillyard, M. H. V. Hoegen, M. Kammler, J. Kaspar, R. Kienberger, P. Krejcik, S. H. Lee, A. M. Lindenberg, B. McFarland, D. Meyer, T. Montagne, E. D. Murray, A. J. Nelson, M. Nicoul, R. Pahl, J. Rudati, H. Schlarb, D. P. Siddons, K. Sokolowski-Tinten, T. Tschentscher, D. von der Linde and J. B. Hastings

Science **315**(5812): 633-636, 2007.

Intense femtosecond laser excitation can produce transient states of matter that would otherwise be inaccessible to laboratory investigation. At high excitation densities, the interatomic forces that bind solids and determine many of their properties can be substantially altered. Here, we present the detailed mapping of the carrier density-dependent interatomic potential of bismuth approaching a solid-solid phase transition. Our experiments combine stroboscopic techniques that use a high-brightness linear electron accelerator-based x-ray source with pulse-by-pulse timing reconstruction for femtosecond resolution, allowing quantitative characterization of the interatomic potential energy surface of the highly excited solid.

Impact Factor: 30.927 Cited Reference Count: 23

Monochromatic electron photoemission from diamondoid monolayers

Yang, W. L., J. D. Fabbri, T. M. Willey, J. R. I. Lee, J. E. Dahl, R. M. K. Carlson, P. R. Schreiner, A. A. Fokin, B. A. Tkachenko, N. A. Fokina, W. Meevasana, N. Mannella, K. Tanaka, X. J. Zhou, T. van Buuren, M. A. Kelly, Z. Hussain, N. A. Melosh and Z. X. Shen

Science **316**(5830): 1460-1462, 2007.

We found monochromatic electron photoemission from large-area self-assembled monolayers of a functionalized diamondoid, [121]tetramantane-6-thiol. Photoelectron spectra of the diamondoid monolayers exhibited a peak at the low-kinetic energy threshold; up to 68% of all emitted electrons were emitted within this single energy peak. The intensity of the emission peak is indicative of diamondoids being negative electron affinity materials. With an energy distribution width of less than 0.5 electron volts, this source of monochromatic electrons may find application in technologies such as electron microscopy, electron beam lithography, and field-emission flat-panel displays.

Impact Factor: 30.028 Cited Reference Count: 23

Experiments and multiscale simulations of laser propagation through ignition-scale plasmas

Glenzer, S. H., D. H. Froula, L. Divol, M. Dorr, R. L. Berger, S. Dixit, B. A. Hammel, C. Haynam, J. A. Hittinger, J. P. Holder, O. S. Jones, D. H. Kalantar, O. L. Landen, A. B. Langdon, S. Langer, B. J. MacGowan, A. J. Mackinnon, N. Meezan, E. I. Moses, C. Niemann, C. H. Still, L. J. Suter, R. J. Wallace, E. A. Williams and B. K. F. Young

Nature Physics **3**(10): 716-719, 2007.

With the next generation of high-power laser facilities for inertial fusion coming online, ensuring laser beam propagation through centimetre-scale plasmas is a key physics issue for reaching ignition. Existing experimental results including the most recent one are limited to small laser spots, low-interaction laser beam energies and small plasma volumes of 1-2 mm. Here, we demonstrate the propagation of an intense, high-energy, ignition-size laser beam through fusion-size plasmas on the National Ignition Facility (NIF) and find the experimental measurements to agree with full-scale modelling. Previous attempts to apply computer modelling as a predictive capability have been limited by the inherently multiscale description of the full laser-plasma interaction processes. The findings of this study validate supercomputer modelling as an essential tool for the design of future ignition experiments.

Impact Factor: 12.040

Formation, stability, and mobility of one-dimensional lipid Bilayers on polysilicon nanowires

Huang, S. C. J., A. B. Artyukhin, J. A. Martinez, D. J. Sirbuly, Y. Wang, J. W. Ju, P. Stroeve and A. Noy

Nano Letters **7**(11): 3355-3359, 2007.

Curved lipid membranes are ubiquitous in living systems and play an important role in many biological processes. To understand how curvature and lipid composition affect membrane formation and fluidity, we have assembled and studied mixed 1,2-dioleoyl-sn-glycero-3-phosphocholine (DOPC) and 1,2-dioleoyl-sn-glycero-3-phosphoethanolamine (DOPE) supported lipid bilayers on amorphous silicon nanowires grown around carbon nanotube cores with controlled wire diameters ranging from 20 to 200 nm. We found that lipid vesicles fused onto nanowire substrates and formed continuous bilayers for all DOPC-DOPE mixtures tested (with the DOPE content of up to 30%). Our measurements demonstrate that nanowire-supported bilayers are mobile, exhibit fast recovery after photobleaching, and have a low concentration of defects. Lipid diffusion coefficients in these high-curvature tubular membranes are comparable to the values reported for flat supported bilayers and increase slightly with decreasing nanowire diameter. A free space diffusion model adequately describes the effect of bilayer curvature on the lipid mobility for nanowire substrates with diameters greater than 50 nm, but shows significant deviations from the experimental values for smaller diameter nanowires.

Impact Factor: 9.960 Cited Reference Count: 37

Ductile crystal line-amorphous nanolaminates

Wang, Y. M., J. Li, A. V. Hamza and T. W. Barbee

Proceedings of the National Academy of Sciences of the United States of America **104**(27): 11155-11160, 2007.

It is known that the room-temperature plastic deformation of bulk metallic glasses is compromised by strain softening and shear localization, resulting in near-zero tensile ductility. The incorporation of metallic glasses into engineering materials, therefore, is often accompanied by complete brittleness or an apparent loss of useful tensile ductility. Here we report the observation of an exceptional tensile ductility in crystalline copper/copper-zirconium glass nanolaminates. These nanocrystalline-amorphous nanolaminates exhibit a high flow stress of 1.09 +/ 0.02 GPa, a nearly elastic-perfectly plastic behavior without necking, and a tensile elongation to failure of 13.8 +/- 1.7%, which is six to eight times higher than that typically observed in conventional crystalline-crystalline nanolaminates (<2%) and most other nanocrystalline materials. Transmission electron microscopy and atomistic simulations demonstrate that shear banding instability no longer afflicts the 5-to 10-nm-thick nanolaminate glassy layers during tensile deformation, which also act as high-capacity sinks for dislocations, enabling absorption of free volume and free energy transported by the dislocations; the amorphous-crystal interfaces exhibit unique inelastic shear (slip) transfer characteristics, fundamentally different from those of grain boundaries. Nanoscale metallic glass layers therefore may offer great benefits in engineering the plasticity of crystalline materials and opening new avenues for improving their strength and ductility.

Impact Factor: 9.643

Structural development of mercaptophenol self-assembled monolayers and the overlying mineral phase during templated CaCO3 crystallization from a transient amorphous film

Lee, J. R. I., T. Y. J. Han, T. M. Willey, D. Wang, R. W. Meulenberg, J. Nilsson, P. M. Dove, L. J. Terminello, T. van Buuren and J. J. De Yoreo

Journal of the American Chemical Society **129**(34): 10370-10381, 2007.

Formation of biomineral structures is increasingly attributed to directed growth of a mineral phase from an amorphous precursor on an organic matrix. While many in vitro studies have used calcite formation on organothiol self-assembled monolayers (SAMs) as a model system to investigate this process, they have generally focused on the stability of amorphous calcium carbonate (ACC) or maximizing control over the order of the final mineral phase. Little is known about the early stages of mineral formation, particularly the structural evolution of the SAM and mineral. Here we use near-edge X-ray absorption spectroscopy (NEXAFS), photoemission spectroscopy (PES), X-ray diffraction (XRD), and scanning electron microscopy (SEM) to address this gap in knowledge by examining the changes in order and bonding of mercaptophenol (MP) SAMs on Au(111) during the initial stages of mineral formation as well as the mechanism of ACC to calcite transformation during template-directed crystallization. We demonstrate that formation of ACC on the MP SAMs brings about a profound change in the morphology of the monolayers: although the as-prepared MP SAMs are composed of monomers with well-defined orientations, precipitation of the amorphous mineral phase results in substantial structural disorder within the monolayers. Significantly, a preferential face of nucleation is observed for crystallization of calcite from ACC on the SAM surfaces despite this static disorder.

Impact Factor: 7.696 Cited Reference Count: 63

Hydrogen encapsulation in a silicon clathrate type I structure: Na-5.5(H-2)(2.15)Si-46: Synthesis and characterization

Neiner, D., N. L. Okamoto, C. L. Condron, Q. M. Ramasse, P. Yu, N. D. Browning and S. M. Kauzlarich

Journal of the American Chemical Society **129**(45): 13857-13862, 2007.

A hydrogen-encapsulated inorganic clathrate, which is stable at ambient temperature and pressure, has been prepared in high yield. Na-5.5(H-2)(2.15)Si-46 is a sodium-deficient, hydrogen-encapsulated, type I silicon clathrate. It was prepared by the reaction between NaSi and NH4Br under dynamic vacuum at 300 degrees C. The Rietveld refinement of the powder X-ray diffraction data is consistent with the clathrate type I structure. The type I clathrate structure has two types of cages where the guest species, in this case Na and H-2, can reside: a large cage composed of 24 Si, in which the guest resides in the 6d crystallographic position, and a smaller one composed of 20 Si, in which the guest occupies the 2a position. Solid-state Na-23, H-1, and Si-29 MAS NMR confirmed the presence of both sodium and hydrogen in the clathrate cages. Na-23 NMR shows that sodium completely fills the small cage and is deficient in the larger cage. The H-1 NMR spectrum shows a pattern consistent with mobile hydrogen in the large cage. Si-29 NMR spectrum is consistent with phase pure type I clathrate framework. Elemental analysis is consistent with the stoichiometry Na-5.5(H-2.15)(2)Si-46. The sodium occupancy was also examined using spherical aberration (Cs) corrected scanning transmission electron microscopy (STEM). The high-angle annular dark-field (HAADF) STEM experimental and simulated images indicated that the Na occupancy of the large cage, 6d sites, is less than 2/3, consistent with the NMR and elemental analysis.

Impact Factor: 7.696 Cited Reference Count: 38

Different apolipoproteins impact nanolipoprotein particle formation

Chromy, B. A., E. Arroyo, C. D. Blanchette, G. Bench, H. Benner, J. A. Cappuccio, M. A. Coleman, P. T. Henderson, A. K. Hinz, E. A. Kuhn, J. B. Pesavento, B. W. Segelke, T. A. Sulchek, T. Tarasow, V. L. Walsworth and P. D. Hoeprich

Journal of the American Chemical Society **129**(46): 14348-14354, 2007.

Spontaneous interaction of purified apolipoproteins and phospholipids results in formation of lipoprotein particles with nanometer-sized dimensions; we refer to these assemblies as nanolipoprotein particles or NLPs. These bilayer constructs can serve as suitable mimetics of biological membranes and are fully soluble in aqueous environments. We made NLPs from dimyristoylphospatidylcholine (DMPC) in combination with each of four different apolipoproteins: apoA-1, Delta-apoA-I fragment, apoE4 fragment, and apolipophorin III (apoLp-III) from the silk moth B. mori. Predominately discoidal in shape, these particles have diameters between 10 and 20 nm, share uniform heights between 4.5 and 5 nm, and can be produced in yields ranging between 40 and 60%. The particular lipoprotein, the lipid to lipoprotein ratio, and the assembly parameters determine the size and homogeneity of nanolipoprotein particles and indicate that apoA-I NLP preparations are smaller than the larger apoE422K and apolp-III NLP preparations.

Impact Factor: 7.696 Cited Reference Count: 29

Experimental observation of quantum confinement in the conduction band of CdSe quantum dots

Lee, J. R. I., R. W. Meulenberg, K. M. Hanif, H. Mattoussi, J. E. Klepeis, L. J. Terminello and T. van Buuren

Physical Review Letters **98**(14), 2007.

X-ray absorption spectroscopy has been used to characterize the evolution in the conduction band (CB) density of states of CdSe quantum dots (QDs) as a function of particle size. We have unambiguously witnessed the CdSe QD CB minimum (CBM) shift to higher energy with decreasing particle size, consistent with quantum confinement effects, and have directly compared our results with recent theoretical calculations. At the smallest particle size, evidence for a pinning of the CBM is presented. Our observations can be explained by considering a size-dependent change in the angular-momentum-resolved states at the CBM.

Impact Factor: 7.489 Cited Reference Count: 23

Observations of plasmons in warm dense matter

Glenzer, S. H., O. L. Landen, P. Neumayer, R. W. Lee, K. Widmann, S. W. Pollaine, R. J. Wallace, G. Gregori, A. Hoell, T. Bornath, R. Thiele, V. Schwarz, W. D. Kraeft and R. Redmer

Physical Review Letters **98**(6), 2007.

We present the first collective x-ray scattering measurements of plasmons in solid-density plasmas. The forward scattering spectra of a laser-produced narrow-band x-ray line from isochorically heated beryllium show that the plasmon frequency is a sensitive measure of the electron density. Dynamic structure calculations that include collisions and detailed balance match the measured plasmon spectrum indicating that this technique will enable new applications to determine the equation of state and compressibility of dense matter.

Impact Factor: 7.489

Competing ordered phases in URu2Si2: Hydrostatic pressure and rhenium substitution

Jeffries, J. R., N. P. Butch, B. T. Yukich and M. B. Maple

Physical Review Letters **99**(21): 4, 2007.

A persistent kink in the pressure dependence of the "hidden order'' (HO) transition temperature of URu2-xRexSi2 is observed at a critical pressure P-c = 15 kbar for 0 <= x <= 0.08. In URu2Si2, the kink at P-c is accompanied by the destruction of superconductivity, a change in the magnitude of a spin excitation gap, determined from electrical resistivity measurements; and a complete gapping of a portion of the Fermi surface (FS), inferred from a change in scattering and the competition between the HO state and superconductivity for FS fraction.

Impact Factor: 7.072 Cited Reference Count: 36

Emergence of strong exchange interaction in the actinide series: The driving force for magnetic stabilization of curium

Moore, K. T., G. van der Laan, R. G. Haire, M. A. Wall, A. J. Schwartz and P. Soderlind

Physical Review Letters **98**(23): 4, 2007.

Using electron energy-loss spectroscopy, many-electron atomic spectral calculations, and density functional theory, we show that angular-momentum coupling in the 5f states plays a decisive role in the formation of the magnetic moment in Cm metal. The 5f states of Cm in intermediate coupling are strongly shifted towards the LS coupling limit due to exchange interaction, unlike most actinide elements where the effective spin-orbit interaction prevails. Hund's rule coupling is the key to producing the large spin polarization that dictates the newly found crystal structure of Cm under pressure.

Impact Factor: 7.072 Cited Reference Count: 26

Demonstration of enhanced radiation drive in hohlraums made from a mixture of high-Z wall materials

Schein, J., O. Jones, M. Rosen, E. Dewald, S. Glenzer, J. Gunther, B. Hammel, O. Landen, L. Suter and R. Wallace

Physical Review Letters **98**(17), 2007.

We present results from experiments, numerical simulations and analytic modeling, demonstrating enhanced hohlraum performance. Care in the fabrication and handling of hohlraums with walls consisting of high-Z mixtures (cocktails) has led to our demonstration, for the first time, of a significant increase in radiation temperature compared to a pure Au hohlraum that is in agreement with predictions and is ascribable to reduced wall losses. The data suggest that a National Ignition Facility ignition hohlraum made of a U:Au:Dy cocktail should have similar to 17% reduction in wall losses compared to a similar gold hohlraum.

Impact Factor: 7.072 Cited Reference Count: 18

Comment on "Symmetry and stability of delta plutonium: The influence of electronic structure" - Reply

Moore, K. T., P. Soderlind and A. J. Schwartz

Physical Review Letters **99**(1): 1, 2007.

Impact Factor: 7.072 Cited Reference Count: 5

Energetic processing of interstellar silicate grains by cosmic rays

Bringa, E. M., S. O. Kucheyev, M. J. Loeffler, R. A. Baragiola, A. Tielens, Z. R. Dai, G. Graham, S. Bajt, J. P. Bradley, C. A. Dukes, T. E. Felter, D. F. Torres and W. van Breugel

Astrophysical Journal **662**(1): 372-378, 2007.

While a significant fraction of silicate dust in stellar winds has a crystalline structure, in the interstellar medium nearly all of it is amorphous. One possible explanation for this observation is the amorphization of crystalline silicates by relatively " low" energy, heavy- ion cosmic rays. Here we present the results of multiple laboratory experiments showing that single- crystal synthetic forsterite (Mg2SiO4) amorphizes when irradiated by 10 MeV Xe ions at large enough fluences. Using modeling, we extrapolate these results to show that 0.1-5.0 GeV heavy-ion cosmic rays can rapidly (similar to 70 Myr) amorphize crystalline silicate grains ejected by stars into the interstellar medium.

Impact Factor: 6.119

New gold and silver-gold catalysts in the shape of sponges and sieves

Jurgens, B., C. Kubel, C. Schulz, T. Nowitzki, V. Zielasek, J. Biener, M. M. Biener, A. V. Hamza and M. Baumer

Gold Bulletin **40**(2): 142-149, 2007.

Gold with a nanoporous sponge-like morphology, generated by leaching of AuAg alloys is presented as a new unsupported material system for catalytic applications. The role of residual silver for catalytic activity towards CO oxidation in the temperature range from -20 to 50 degrees C has been investigated by comparison with Au and Au/Ag zeolite catalysts. As revealed by a systematic variation of the silver content in the zeolite catalysts, bimetallic systems exhibit a significantly higher activity than pure gold, probably due to activation/dissociation of molecular oxygen by silver. By STEM tomography we can unambiguously prove that at least some of the particles form inside the zeolite lattice.

Impact Factor: 6.029 Cited Reference Count: 45

Lanthanum hexaboride nanoobelisks

Brewer, J. R., N. Deo, Y. M. Wang and C. L. Cheung

Chemistry of Materials **19**(26): 6379-6381, 2007.

Impact Factor: 5.104 Cited Reference Count: 21

Germanium nanocrystals synthesized in high-boiling-point organic solvents

Zaitseva, N., Z. R. Dai, C. D. Grant, J. Harper and C. Saw

Chemistry of Materials **19**(21): 5174-5178, 2007.

Ge nanoparticles with sizes from 1 to 15 nm were synthesized by thermal decomposition of the germane precursors trichlorogermane, tetraethylgermane, and tetrabutylgermane. Experiments were performed in the organic solvents trioctylamine, squalene, and octacosane, which have boiling points in the temperature range from 380 to 429 degrees C. The use of high-boiling-point solvents extended the temperature range of the reactions, thus enabling the experiments to be conducted with organogermane precursors which have high decomposition points above 400 degrees C. Characterization by X-ray diffraction and transmission electron microscopy showed that, depending on the reaction temperature, the final decomposition products consist of amorphous Ge nanoparticles, nanocrystals, or nanowires that grow only in the (110) direction.

Impact Factor: 5.104 Cited Reference Count: 20

Correlation spectroscopy of minor fluorescent species: Signal purification and distribution analysis

Laurence, T. A., Y. Kwon, E. Yin, C. W. Hollars, J. A. Camarero and D. Barsky

Biophysical Journal **92**(6): 2184-2198, 2007.

We are performing experiments that use fluorescence resonance energy transfer (FRET) and fluorescence correlation spectroscopy (FCS) to monitor the movement of an individual donor-labeled sliding clamp protein molecule along acceptor-labeled DNA. In addition to the FRET signal sought from the sliding clamp-DNA complexes, the detection channel for FRET contains undesirable signal from free sliding clamp and free DNA. When multiple fluorescent species contribute to a correlation signal, it is difficult or impossible to distinguish between contributions from individual species. As a remedy, we introduce "purified FCS", which uses single molecule burst analysis to select a species of interest and extract the correlation signal for further analysis. We show that by expanding the correlation region around a burst, the correlated signal is retained and the functional forms of FCS fitting equations remain valid. We demonstrate the use of purified FCS in experiments with DNA sliding clamps. We also introduce "single-molecule FCS", which obtains diffusion time estimates for each burst using expanded correlation regions. By monitoring the detachment of weakly-bound 30-mer DNA oligomers from a single-stranded DNA plasmid, we show that single-molecule FCS can distinguish between bursts from species that differ by a factor of 5 in diffusion constant.

Impact Factor: 4.507 Cited Reference Count: 31

Growth and structure of PbVO3 thin films

Martin, L. W., Q. Zhan, Y. Suzuki, R. Ramesh, M. F. Chi, N. Browning, T. Mizoguchi and J. Kreisel

Applied Physics Letters **90**(6), 2007.

Multifunctional materials promise to provide the foundation for a new class of devices in which functional properties are coupled to one another. Examples include magnetoelectric materials in which magnetic and ferroelectric properties are coupled. Here the authors report the successful growth of single phase, fully epitaxial thin films of the multifunctional material, PbVO3, using pulsed laser deposition. This growth offers an alternative means for the production of PbVO3 outside of high-temperature and high-pressure techniques through growth of epitaxial thin films on various substrates. The structure of this highly distorted perovskite is examined using x-ray diffraction, Raman spectroscopy, and transmission electron microscopy. (c) 2007 American Institute of Physics.

Impact Factor: 4.127

Prospects for electron imaging with ultrafast time resolution

Armstrong, M. R., B. W. Reed, B. R. Torralva and N. D. Browning

Applied Physics Letters **90**(11), 2007.

Many pivotal aspects of material science, biomechanics, and chemistry would benefit from nanometer imaging with ultrafast time resolution. Here the authors demonstrate the feasibility of short-pulse electron imaging with 10 nm/10 ps spatiotemporal resolution, sufficient to characterize phenomena that propagate at the speed of sound in materials (1-10 km/s) without smearing. The authors outline resolution-degrading effects that occur at high current density followed by strategies to mitigate these effects. Finally, the authors present a model electron imaging system that achieves 10 nm/10 ps spatiotemporal resolution. (c) 2007 American Institute of Physics.

Impact Factor: 4.127 Cited Reference Count: 32

Evaluation of UV absorption coefficient in laser-modified fused silica

Negres, R. A., M. W. Burke, S. B. Sutton, P. DeMange, M. D. Feit and S. G. Demos

Applied Physics Letters **90**(6), 2007.

Laser-induced damage in transparent dielectrics leads to the formation of laser-modified material as a result of exposure to extreme localized temperatures and pressures. In this work, an infrared thermal imaging system in combination with a fluorescence microscope is used to map the dynamics of the local surface temperature and fluorescence intensity under cw, UV excitation of laser-modified fused silica within a damage site. The energy deposited via linear absorption mechanisms and the absorption coefficient of the modified material are estimated based on a thermal diffusion model. In addition, irreversible changes in the absorption following extended laser exposure were observed.

Impact Factor: 4.127

Vapor pressure and sublimation rate of molecular crystals: Role of internal degrees of freedom

Maiti, A., L. A. Zepeda-Ruiz, R. H. Gee and A. K. Burnham

Journal of Physical Chemistry B **111**(51): 14290-14294, 2007.

It is a common practice to approximate the desorption rate of atoms from crystal surfaces with an expression of the form v(eff) exp(-Delta E/k(B)T), where Delta E is an activation barrier to desorb and v(eff) is an effective vibrational frequency similar to 10(12) S-1. For molecular solids, however, such an approximation can lead to a many orders of magnitude underestimation of vapor pressure and sublimation rates due to neglected contributions from molecular internal degrees of freedom. Here, we develop a simple working formula that yields good estimates for a general molecular (or atomic) solid and illustrate the approach by computing equilibrium vapor pressure of three different molecular solids and an atomic solid, as well as the desorption rate of a foreign (inhibitor) molecule from the surface of a molecular solid.

Impact Factor: 4.115 Cited Reference Count: 26

Effects of carbon on ion-implantation-induced disorder in GaN

Kucheyev, S. O., J. E. Bradby, C. P. Li, S. Ruffell, T. van Buuren and T. E. Felter

Applied Physics Letters **91**: 261905, 2007.

Wurtzite GaN films bombarded with 40 keV C ions to high doses (5x10(17) and 1x10(18) cm(-2)) are studied by a combination of Rutherford backscattering/channeling spectrometry, transmission electron microscopy, and soft x-ray absorption spectroscopy. Results show that, contrary to other ion species, implanted C forms nitrilelike carbon-nitride bonds (-C equivalent to N) and suppresses ion-beam-induced material decomposition involving the formation and agglomeration of greater than or similar to 5-nm-large N-2 gas bubbles. (c) 2007 American Institute of Physics.

Impact Factor: 3.977 Cited Reference Count: 22

Segregation and precipitation of Er in Ge

Kucheyev, S. O., J. E. Bradby, S. Ruffell, C. P. Li, T. E. Felter and A. V. Hamza

Applied Physics Letters **90**(22): 21901-21901, 2007.

Although Er-doped Ge nanomaterials are attractive for photonic applications, very little is known about the basic properties of Er in Ge. Here, the authors study the annealing behavior of Ge implanted with keV Er ions to doses resulting in less than or similar to 1 at. % of Er. Large redistribution of Er, with segregation at the amorphous/crystalline interface, starts at greater than or similar to 500 degrees C, while lower temperatures are required for material recrystallization. However, even at 400 degrees C, Er forms precipitates. The concentration of Er trapped in the bulk after recrystallization decreases with increasing temperature but is independent of the initial bulk Er concentration for the range of ion doses studied here. (C) 2007 American Institute of Physics.

Impact Factor: 3.977

Incipient plasticity in metallic glass modulated nanolaminates

Wang, Y. M., A. V. Hamza and T. W. Barbee

Applied Physics Letters **91**(6): 61924-61924, 2007.

The plastic deformation in copper-zirconium nanocrystalline-amorphous nanolaminates is investigated by means of stress-relaxation experiments at a range of initial stress levels. Progressive multistep relaxation cycles reveal that the onset of plastic deformation occurs at a much lower stress level in nanocrystalline-amorphous nanolaminate than in crystalline-crystalline nanolaminates or other nanostructured materials. The derived activation volumes and strain rate sensitivities imply interfacial dislocation mechanisms, consistent with the observations from postmorterm transmission electron microscopy. This indicates that the crystalline-amorphous interfaces may be the preferred source for dislocation nucleation and/or emission.

Impact Factor: 3.977

Mechanical response of freestanding Au nanopillars under compression

Zepeda-Ruiz, L. A., B. Sadigh, J. Biener, A. M. Hodge and A. V. Hamza

Applied Physics Letters **91**: 101907, 2007.

We employ molecular dynamics simulations of defect-free nanopillars with realistic cylindrical geometries to obtain an atomic-level picture of their deformation behavior under compression. We find that dislocations are nucleated in the two outermost surface layers. Furthermore, plastic yield depends crucially on the particular arrangement of steps and facets at the surface of the nanopillars. We show that different facet orientations can differ dramatically in their response to external stresses. Freestanding nanopillars exhibit a highly nonuniform distribution of stresses along their height. This causes an elastic deformation that leads to a barrel-like shape attained by the nanopillars under compression. The stress concentration at the center of the pillars due to barreling causes dislocations to preferentially nucleate in this region.

Impact Factor: 3.977

Structure of low-density nanoporous dielectrics revealed by low-vacuum electron microscopy and small-angle X-ray scattering

Kucheyev, S. O., M. Toth, T. F. Baumann, A. V. Hamza, J. Ilavsky, W. R. Knowles, C. K. Saw, B. L. Thiel, V. Tileli, T. van Buuren, Y. M. Wang and T. M. Willey

Langmuir **23**(2): 353-356, 2007.

Aerogels (AGs) are ultralow-density nanoporous solids that have numerous potential applications. However, as most AGs are strong insulators with poor mechanical properties, direct studies of the complex nanoporous structure of AGs by methods such as atomic force and conventional scanning electron microscopy (SEM) have not proven feasible. Here, we use low-vacuum SEM to image directly the ligament and pore size and shape distributions of representative AGs over a wide range of length scales (similar to 10(0)-10(5) nm). The structural information obtained is used for unambiguous, real-space interpretation of small-angle X-ray scattering curves for these complex nanoporous systems. Low-vacuum SEM permits imaging of both cross-sections and skin layers of AG monoliths. Images of skin layers reveal the presence of microcracks, which alter the properties of cast monolithic AGs.

Impact Factor: 3.705 Cited Reference Count: 23

Investigation of signal dependence on tissue thickness in near infrared spectral imaging

Lin, B., V. Chernomordik, A. Gandjbakhche, D. Matthews and S. Demos

Optics Express **15**(25): 16581-16595, 2007.

The signal intensity in near infrared autofluorescence and polarization sensitive light scattering imaging is explored as a function of tissue thickness using homogeneous porcine cardiac tissue samples as a model system. Eight images are recorded from each tissue sample including two autofluorescence images obtained under 408 nm and 633 nm excitation and six light scattering images acquired with alternating linear polarization orientations (parallel or perpendicular) under 700 nm, 850 nm, and 1000 nm linearly polarized illumination. The mean image intensity of each sample for each imaging method is plotted as a function of tissue thickness. The experimental results indicate a strong dependence of the detected signal on tissue thickness up to approximately 2 mm. Furthermore, the intensity of the spectral ratio images also exhibit thickness-dependent changes up to about 3 mm. The behavior of the light scattering experimental data was reproduced using a mathematical model based on a modified version of the random walk theory of photon migration. (C) 2007 Optical Society of America.

Impact Factor: 3.598 Cited Reference Count: 23

Strong UV absorption and visible luminescence in ytterbium-doped aluminosilicate glass under UV excitation

Engholm, M., L. Norin and D. Aberg

Optics Letters **32**(22): 3352-3354, 2007.

A broad visible luminescence band and characteristic IR luminescence of Yb3+ ions are observed under UV excitation in ytterbium-doped aluminosilicate glass. Samples made under both oxidizing and reducing conditions are analyzed. A strong charge-transfer absorption band in the UV range is observed for glass samples containing ytterbium. Additional absorption bands are observed for the sample made under reducing conditions, which are associated with f - d transitions of divalent ytterbium. The visible luminescence band is attributed to 5d - 4f emission from Yb2+ ions, and the IR luminescence is concluded to originate from a relaxed charge-transfer transition. The findings are important to explain induced optical losses (photodarkening) in high-power fiber lasers. (c) 2007 Optical Society of America.

Impact Factor: 3.598 Cited Reference Count: 15

High-cycle fatigue of nickel-base superalloy Rene 104 (ME3): Interaction of microstructurally small cracks with grain boundaries of known character

Gao, Y., J. S. Stolken, M. Kumar and R. O. Ritchie

Acta Materialia **55**(9): 3155-3167, 2007.

High-cycle fatigue (HCF), involving the premature initiation and/or rapid propagation of small cracks to failure due to high-frequency cyclic loading, has been identified as one of the leading causes of turbine engine failures in aircraft. In this work, we consider the feasibility of using grain-boundary engineering to improve the HCF properties of a polycrystalline nickel-base superalloy, Rene 104 (also known as ME3), through systematic modification of the grain-boundary distribution. In particular, we investigate the growth of microstructurally small fatigue cracks at ambient temperature in microstructures with varying proportions of “special” vs. “random” boundaries, as defined by coincident-site lattice theory. Specifically, we examine the interaction of propagating small (similar to 10-900 mu m) surface cracks with grain boundaries of known character, with respect both to any deflection in crack trajectory that occurs at or near the boundary, and more importantly to any local changes in crack-growth rates. In addition, finite-element calculations are performed to evaluate the effective driving force and plastic-zone profile for such small-crack propagation, incorporating information from both the local microstructure (from electron backscattering diffraction scans) and the surface crack-path profile.

Impact Factor: 3.549 Cited Reference Count: 35

Rapid phase transformation kinetics on a nanoscale: Studies of the alpha -> beta transformation in pure, nanocrystalline Ti using the nanosecond dynamic transmission electron microscope

LaGrange, T., G. H. Campbell, P. E. A. Turchi and W. E. King

Acta Materialia **55**(15): 5211-5224, 2007.

Using the unique capabilities and high time resolution of dynamic transmission electron microscopy (DTEM), the fast kinetics of alpha -> beta-phase transformation in nanocrystalline Ti films were investigated using single-shot electron diffraction and bright-field TEM images. From quantitative analysis of the diffraction patterns, the transformation rates were determined for temperatures between transition start (1155 K) and melt temperature (1943 K). The experimental data were summarized in a time-temperature-transformation (TTT) curve with nanosecond time resolution. Theoretical TTT curves were calculated using analytical models for isothermal martensite and available thermodynamic data. Above 1300 K, there is excellent agreement between the experiment and the discrete-obstacle interaction model, suggesting that the nucleation rate and thermally assisted motion of the martensite interface are controlled by interface-solute atom interactions. However, theory predicts much slower transformation rates near the transition temperature than experiment. Experimental data fits using the Pati-Cohen model suggests that an increase in autocatalytic nucleation may partially account for the fast transformation rates at lower temperatures. Published by Elsevier Ltd on behalf of Acta Materialia Inc.

Impact Factor: 3.549

A viscoplastic micromechanical model for the yield strength of nanocrystalline materials

Lebensohn, R. A., E. M. Bringa and A. Caro

Acta Materialia **55**(1): 261-271, 2007.

In this paper we present a micromechanical approach based on fast Fourier transforms to study the role played by dislocation glide and grain boundary (GB) accommodation in the determination of the plastic behavior of nanostructured materials. For this, we construct unit cells representing self-similar polycrystals with different grain sizes in the nanometer range and use local constitutive equations for slip and GB accommodation. We study the effect of grain size, strain rate and pressure on the local and effective behavior of nanostructured Ice materials with parameters obtained from experiments and atomistic simulations. Predictions of a previous qualitative pressure-sensitive model for the effective yield strength behind a shock front are substantially improved by considering strain partition between slip and GB activity. Under quasiestatic conditions, assuming diffusion-controlled mechanisms at GB, the model predicts a strain-rate sensitivity increase in nanocrystalline samples with respect to the coarse-grained material of the same order as in recently published experiments.

Impact Factor: 3.430 Cited Reference Count: 51

Phase-field modelling and synchrotron validation of phase transformations in martensitic dual-phase steel

Thiessen, R. G., J. Sietsma, T. A. Palmer, J. W. Elmer and I. M. Richardson

Acta Materialia **55**(2): 601-614, 2007.

A thermodynamically based method to describe the phase transformations during heating and cooling of martensitic dual-phase steel has been developed, and in situ synchrotron measurements of phase transformations have been undertaken to support the model experimentally. Nucleation routines are governed by a novel implementation of the classical nucleation theory in a general phase-field code. Physically-based expressions for the temperature-dependent interface mobility and the driving forces for transformation have also been constructed. Modelling of martensite was accomplished by assuming a carbon supersaturation of the body-centred-cubic ferrite lattice. The simulations predict kinetic aspects of the austenite formation during heating and ferrite formation upon cooling. Simulations of partial austenitising thermal cycles predicted peak and retained austenite percentages of 38.2% and 6.7%, respectively, while measurements yielded peak and retained austenite percentages of 31.0% and 7.2% (+/- 1%). Simulations of a complete austenitisation thermal cycle predicted the measured complete austenitisation and, upon cooling, a retained austenite percentage of 10.3% while 9.8% (+/- 1%) retained austenite was measured. (c) 2006 Acta Materialia Inc. Published by Elsevier Ltd. All rights reserved.

Impact Factor: 3.430 Cited Reference Count: 23

Scaling equation for yield strength of nanoporous open-cell foams

Hodge, A. M., J. Biener, J. R. Hayes, P. M. Bythrow, C. A. Volkert and A. V. Hamza

Acta Materialia **55**(4): 1343-1349, 2007.

A comprehensive study on the relationship between yield strength, relative density and ligament sizes is presented for nanoporous An foams. Depth-sensing nanoindentation tests were performed on nanoporous foams ranging from 20% to 42% relative density with ligament sizes ranging from 10 to 900 nm. The Gibson and Ashby yield strength equation for open-cell macrocellular foams is modified in order to incorporate ligament size effects. This study demonstrates that, at the nanoscale, foam strength is governed by ligament size, in addition to relative density. Furthermore, we present the ligament length scale as a new parameter to tailor foam properties and achieve high strength at low densities. (c) 2006 Acta Materialia Inc. Published by Elsevier Ltd. All rights reserved.

Impact Factor: 3.430

Equation of state of solid nickel aluminide

Swift, D. C., D. L. Paisley, K. J. McClellan and G. J. Ackland

Physical Review B **76**(13): 15, 2007.

The pressure-volume-temperature equation of state of the intermetallic compound NiAl was calculated theoretically, and compared with experimental measurements. Electron ground states were calculated for NiAl in the CsCl structure, using ab initio pseudopotentials and density functional theory (DFT), and were used to predict the cold compression curve and the density of phonon states. It was desirable to interpolate and smooth the cold compression states; the Rose form of compression curve was found to reproduce the ab initio calculations well in compression but exhibited significant deviations in expansion. A thermodynamically complete equation of state was constructed for NiAl, which overpredicted the mass density at standard temperature and pressure (STP) by 4%, fairly typical for predictions based on DFT. A minimally adjusted equation of state was constructed by tilting the cold compression energy-volume relation by similar to 7 GPa to reproduce the observed STP mass density. Shock waves were induced in crystals of NiAl by the impact of laser-launched Cu flyers and by launching NiAl flyers into transparent windows of known properties. The TRIDENT laser was used to accelerate the flyers, 5 mm in diameter and 100-400 mu m thick, to speeds between 100 and 600 m/s. Point and line-imaging laser Doppler velocimetry was used to measure the acceleration of the flyer and the surface velocity history of the target. The velocity histories were used to deduce the stress state, and hence states on the principal Hugoniot and the flow stress. Flyers and targets were recovered from most experiments. The effect of elasticity and plastic flow in the sample and window was assessed. The ambient isotherm reproduced static compression data very well, and the predicted Hugoniot was consistent with shock compression data.

Impact Factor: 3.185 Cited Reference Count: 40

Diffusion mechanisms of native point defects in rutile TiO2: Ab initio total-energy calculations

Iddir, H., S. Ogut, P. Zapol and N. D. Browning

Physical Review B **75**(7), 2007.

The structural energetics and diffusion mechanisms of the two most important point defects in rutile TiO2, the oxygen vacancy (V-O) and the titanium interstitial (Ti-I), are examined using the ab initio pseudopotential total-energy method. The two defects are found to be somewhat competitive in energy, with V-O being more favorable in a larger range of the stoichiometry. The Ti-I, on the other hand, is shown to be the major diffusive species, since its low migration barrier is significantly smaller (by similar to 1 eV) compared to that of V-O. The diffusion mechanisms of Ti-I parallel and perpendicular to the crystal c axis are found to be different with a surprisingly larger barrier along the more open [001] direction, which was originally thought to be the easier channel for Ti self-diffusion. These theoretical findings are in excellent quantitative agreement with existing experimental data.

Impact Factor: 3.185

Simulations of the mechanical properties of crystalline, nanocrystalline, and amorphous SiC and Si

Ivashchenko, V. I., P. E. A. Turchi and V. I. Shevchenko

Physical Review B **75**(8), 2007.

Molecular-dynamics simulations of crystalline (c), nanocrystalline (nc), and amorphous (a) silicon carbides and silicon were carried out to investigate their vibrational and mechanical properties. The atomic configurations, vibrational spectra, and stress-strain curves were calculated at room temperature. In the case of the nanocrystalline structures, these characteristics were analyzed as functions of grain size. Young's and bulk modul and yield and flow stresses were determined from uniaxial deformation of samples under periodic boundary constraints and from experiments on rod extension. For silicon carbides, Young's modulus and flow stress decrease in the sequence "c-nc-a," and with decreasing grain size, which is attributed to a weakening of the Si-C bonds in the amorphous matrix. The enhancement of the strength properties of the homopolar nc-Si structures is attributed to their deformation anisotropy. The calculated vibrational spectra and Young's moduli are in rather good agreement with the corresponding experimental characteristics.

Impact Factor: 3.185

Shock and release temperatures in molybdenum: Experiment and theory

Swift, D. C., A. Seifter, D. B. Holtkamp and D. A. Clark

Physical Review B **76**(5): -, 2007.

Shock and release temperatures in Mo were calculated, taking heating from plastic flow predicted using the Steinberg-Guinan model into account. Plastic flow was calculated self-consistently with the shock jump conditions: this is necessary for a rigorous estimate of the locus of shock states accessible. Plastic heating increased monotonically with shock pressure and subsequent release, reaching an estimated 50 K at a pressure of 60 GPa, and around 120 K on release to zero pressure. The temperatures were compared with surface emission spectrometry measurements for Mo shocked to around 60 GPa and then released into vacuum or into a LiF window. Shock loading was induced by the impact of a planar projectile, accelerated by high explosive or in a gas gun. Surface velocimetry showed an elastic wave at the start of release from the shocked state; the amplitude of the elastic wave matched the prediction to around 10%, indicating that the predicted flow stress in the shocked state was reasonable. The measured temperatures were consistent with the simulations, indicating that the fraction of plastic work converted to heat was in the range 70%-100% for these loading conditions. The shock temperature predicted with plastic heating was consistent with a reanalyzed temperature from neutron resonance spectrometry.

Impact Factor: 3.185 Cited References Count:28

Electronic structure of nanoporous ceria from x-ray absorption spectroscopy and atomic multiplet calculations

Kucheyev, S. O., B. J. Clapsaddle, Y. M. Wang, T. van Buuren and A. V. Hamza

Physical Review B **76**(23): 5420-5420, 2007.

We study the electronic structure of three-dimensional nanoporous CeO2-x monoliths (aerogels) by soft x-ray absorption near-edge structure (XANES) spectroscopy. Atomic multiplet calculations are used to interpret high-resolution Ce M-4,M-5- and N-4,N-5-edge XANES spectra. Results show that aerogels with thicker ligaments, but with the same average size of crystallites, exhibit larger Ce3+ content and, hence, higher oxygen deficiency.

Impact Factor: 3.107 Cited Reference Count: 34

Dislocation nucleation in bcc Ta single crystals studied by nanoindentation

Biener, M. M., J. Biener, A. M. Hodge and A. V. Hamza

Physical Review B **76**(16): 6, 2007.

The study of dislocation nucleation in close-packed metals by nanoindentation has recently attracted much interest. Here, we address the peculiarities of the incipient plasticity in body centered cubic (bcc) metals using low index Ta single crystals as a model system. The combination of nanoindentation with high-resolution atomic force microscopy provides us with experimental atomic-scale information on the process of dislocation nucleation and multiplication. Our results reveal a unique deformation behavior of bcc Ta at the onset of plasticity, which is distinctly different from that of close-packed metals. Most noticeably, we observe only one rather than a sequence of discontinuities in the load-displacement curves. This and other differences are discussed in the context of the characteristic plastic deformation behavior of bcc metals.

Impact Factor: 3.107 Cited Reference Count: 40

Cubic Laves ferromagnet TbNi2Mn investigated through ambient-pressure magnetization and specific heat and high pressure ac magnetic susceptibility

Jackson, D. D., S. K. McCall, S. T. Weir, A. B. Karki, D. P. Young, W. Qiu and Y. K. Vohra

Physical Review B **75**(22): 8, 2007.

TbNi2Mn is a cubic Laves material, isostructural to TbNi2, with the Mn sitting on both the Tb and the Ni lattice positions. It is ferromagnetic at ambient pressure at T-C=151 K and has been investigated in detail at ambient pressure through magnetization and specific heat with various applied magnetic fields. It displays Curie-Weiss behavior above T-C, with an effective moment of 8.43 mu(B)/f.u., and isothermal magnetization at various temperatures is consistent with narrow domain walls. The low-temperature specific heat results in a linear contribution of 65 mJ/mol K-2 and a Debye temperature of theta(D)=188 K. The ac magnetic susceptibility has been investigated using designer diamond anvils up to 28.3 GPa. A magnetic anomaly at T-* is investigated as a function of both magnetic field and pressure, both of which have very little effect for fields less than the coercive force. The Curie temperature decreases at a rate of dT(C)/dP=-1.96 K/GPa, and differences between hydrostatic and nonhydrostatic conditions are discussed.

Impact Factor: 3.107 Cited Reference Count: 36

Annealing twins in nanocrystalline fcc metals: A molecular dynamics simulation

Farkas, D., E. Bringa and A. Caro

Physical Review B **75**(18): 5, 2007.

We report fully three-dimensional atomistic molecular dynamics studies of grain growth kinetics in nanocrystalline Cu of 5 nm average grain size. We observe the formation of annealing twins as part of the grain growth process. The grain size and energy evolution was monitored as a function of time for various temperatures, yielding an activation energy for the process. The atomistic mechanism of annealing twin formation from the moving boundaries is described.

Impact Factor: 3.107 Cited Reference Count: 35

Unconventional ferrimagnetic ordering of Ce in the anisotropic metal CeCrSb3

Jackson, D. D., S. K. McCall, A. B. Karki and D. P. Young

Physical Review B **76**(6): 5, 2007.

We report on the magnetization and electrical resistivity on single crystals of CeCrSb3, a ferromagnetic metal with large anisotropy. It undergoes two ferromagnetic transitions: the first is at T-Cr=115 K due to the electrons from the Cr ions and the second is a gradual alignment of the Ce3+ 4f electrons between 48 and 18 K. The Cr moments behave similarly in LaCrSb3, with the easy axis along the b axis. Below 48 K, the Ce moments begin to align along the c axis, and as the applied field increases, their effect on the magnetization increases in importance, resulting in nearly linear behavior of M-c(T) for H=30 kG. At 5 K, the saturation moment along the c axis is 3.28 mu(B)/f.u., and along the b axis, the magnetization saturates to 1.29 mu(B)/f.u., the difference being only 7% less than the predicted Hund's rule value for Ce3+, indicating that the 4f moments have fully aligned along the c axis.

Impact Factor: 3.107 Cited Reference Count: 20

Quantifying structural damage from self-irradiation in a plutonium superconductor

Booth, C. H., E. D. Bauer, M. Daniel, R. E. Wilson, J. N. Mitchell, L. A. Morales, J. L. Sarrao and P. G. Allen

Physical Review B **76**(6): 7, 2007.

The 18.5 K superconductor PuCoGa5 has many unusual properties, including those due to damage induced by self-irradiation. The superconducting transition temperature decreases sharply with time, suggesting a radiation-induced Frenkel defect concentration much larger than predicted by current radiation damage theories. Extended x-ray absorption fine-structure measurements demonstrate that while the local crystal structure in fresh material is well ordered, aged material is disordered much more strongly than expected from simple defects, consistent with strong disorder throughout the damage cascade region. These data highlight the potential impact of local lattice distortions relative to defects on the properties of irradiated materials and underscore the need for more atomic-resolution structural comparisons between radiation damage experiments and theory.

Impact Factor: 3.107

Association of oxygen vacancies with impurity metal ions in lead titanate

Erhart, P., R. A. Eichel, P. Traskelin and K. Albe

Physical Review B **76**(17): 4116, 2007.

Thermodynamic, structural, and electronic properties of isolated copper and iron atoms as well as their complexes with oxygen vacancies in tetragonal lead titanate are investigated by means of first principles calculations. Both dopants exhibit a strong chemical driving force for the formation of M-Ti-V-O (M=Cu,Fe) defect associates. The most stable configurations correspond to a local dipole aligned along the tetragonal axis parallel to the spontaneous polarization. Local spin moments are obtained and the calculated spin densities are discussed. The calculations provide a simple and consistent explanation for the experimental findings. The results are discussed in the context of models for degradation of ferroelectric materials.

Impact Factor: 3.107

Annealing twins in nanocrystalline fcc metals: A molecular dynamics simulation

Farkas, D., E. Bringa and A. Caro

Physical Review B **75**(18): 4111-4111, 2007.

We report fully three-dimensional atomistic molecular dynamics studies of grain growth kinetics in nanocrystalline Cu of 5 nm average grain size. We observe the formation of annealing twins as part of the grain growth process. The grain size and energy evolution was monitored as a function of time for various temperatures, yielding an activation energy for the process. The atomistic mechanism of annealing twin formation from the moving boundaries is described.

Impact Factor: 3.107

Rampant changes in 5f(5/2) and 5f(7/2) filling across the light and middle actinide metals: Electron energy-loss spectroscopy, many-electron atomic spectral calculations, and spin-orbit sum rule

Moore, K. T., G. van der Laan, M. A. Wall, A. J. Schwartz and R. G. Haire

Physical Review B **76**(7): 3105-3105, 2007.

We examine the branching ratio of the N-4,N-5 (4d -> 5f) spectra of Th, U, Np, Pu, Am, and Cm metals using electron energy-loss spectroscopy (EELS) in a transmission electron microscope, together with many-electron atomic spectral calculations and the spin-orbit sum rule. Our results show the following. (1) The actinide metals Pu, Am, and Cm exhibit intermediate coupling. (2) The intermediate coupling values for the 5f states as calculated using a many-electron atomic model are correct for the actinides; this being proven by our results for curium. (3) The EELS branching ratio is sensitive to the degree of 5f electron delocalization, which is illustrated by the transition from LS to intermediate coupling between U and Pu.

Impact Factor: 3.107

Ruthenium/aerogel nanocomposites via atomic layer deposition

Biener, J., T. F. Baumann, Y. M. Wang, E. J. Nelson, S. O. Kucheyev, A. V. Hamza, M. Kemell, M. Ritala and M. Leskela

Nanotechnology **18**(5), 2007.

We present a general approach to prepare metal/aerogel nanocomposites via template directed atomic layer deposition (ALD). In particular, we used a Ru ALD process consisting of alternating exposures to bis(cyclopentadienyl) ruthenium (RuCp2) and air at 350 degrees C to deposit metallic Ru nanoparticles on the internal surfaces of carbon and silica aerogels. The technique does not affect the morphology of the aerogel template and offers excellent control over metal loading by simply adjusting the number of ALD cycles. We also discuss the limitations of our ALD approach and suggest ways to overcome these.

Impact Factor: 2.993 Cited Reference Count: 34

Using noninvasive multispectral imaging to quantitatively assess tissue vasculature

Vogel, A., V. V. Chernomordik, J. D. Riley, M. Hassan, F. Amyot, B. Dasgeb, S. G. Demos, R. Pursley, R. F. Little, R. Yarchoan, Y. Tao and A. H. Gandjbakhche

Journal of Biomedical Optics **12**(5): 13, 2007.

This research describes a noninvasive, noncontact method used to quantitatively analyze the functional characteristics of tissue. Multispectral images collected at several near-infrared wavelengths are input into a mathematical optical skin model that considers the contributions from different analytes in the epidermis and dermis skin layers. Through a reconstruction algorithm, we can quantify the percent of blood in a given area of tissue and the fraction of that blood that is oxygenated. Imaging normal tissue confirms previously reported values for the percent of blood in tissue and the percent of blood that is oxygenated in tissue and surrounding vasculature, for the normal state and when ischemia is induced. This methodology has been applied to assess vascular Kaposi's sarcoma lesions and the surrounding tissue before and during experimental therapies. The multispectral imaging technique has been combined with laser Doppler imaging to gain additional information. Results indicate that these techniques are able to provide quantitative and functional information about tissue changes during experimental drug therapy and investigate progression of disease before changes are visibly apparent, suggesting a potential for them to be used as complementary imaging techniques to clinical assessment. (c) 2007 Society of Photo-Optical Instrumentation Engineers.

Impact Factor: 2.870 Cited Reference Count: 30

Counting constituents in molecular complexes by fluorescence photon antibunching

Fore, S., T. A. Laurence, C. W. Hollars and T. Huser

IEEE Journal of Selected Topics in Quantum Electronics **13**(4): 996-1005, 2007.

Modern single molecule fluorescence microscopy offers new, highly quantitative ways for studying the systems biology of cells while keeping the cells healthy and alive in their natural environment. In this context, a quantum optical technique, photon antibunching, has found a small niche in the continuously growing applications of single molecule techniques to characterize small molecular complexes. Here, we review some of the most recent applications of photon antibunching in biophotonics research, and we provide a guide for how to conduct photon antibunching experiments at the single molecule level by applying techniques borrowed from time-correlated single photon counting (TCSPC). We provide a number of new examples for applications of photon antibunching to the study of multichromophoric, molecules and small molecular complexes.

Impact Factor: 2.842 Cited Reference Count: 58

Depth-dependent mechanical properties of enamel by nanoindentation

Zhou, J. and L. L. Hsiung

Journal of Biomedical Materials Research Part A **81**A(1): 66-74, 2007.

Nanoindentation has recently emerged to be the primary method to study the mechanical behavior and reliability of human enamel. Its hardness and elastic modulus were generally reported as average values with standard deviations that were calculated from the results of multiple nanoindentation testing. In such an approach, it is assumed that the mechanical properties of human enamel are constant, independent of testing parameters, like indent depth and loading rate. However, little is known if they affect the measurements. In this study, we investigated the dependence of the hardness and elastic modulus of human enamel on the indent depth. We found that in a depth range from 100 to 2000 nm the elastic moduli continuously decreased from similar to 104 to 70 GPa, and the hardnesses decreased from similar to 5.7 to 3.6 GPa. We then considered human enamel as a fiber-reinforced composite, and used the celebrated rule of mixture theory to quantify the upper and lower bounds of the elastic moduli, which were shown to cover the values measured in the current study and previous studies. Accordingly, we attributed the depth dependence of the hardness and modulus to the continuous microstructure evolution induced by the nanoindenter tip. (c) 2006 Wiley Periodicals, Inc. J Biomed Mater Res 81A: 66-74, 2007.

Impact Factor: 2.743 Cited Reference Count: 23

Peptide stabilized amphotericin B nanodisks

Tufteland, M., J. B. Pesavento, R. L. Bermingham, P. D. Hoeprich and R. O. Ryan

Peptides **28**(4): 741-746, 2007.

Nanometer scale apolipoprotein A-I stabilized phospholipid disk complexes (nanodisks; ND) have been formulated with the polyene antibiotic amphotericin B (AMB). The present studies were designed to evaluate if a peptide can substitute for the function of the apolipoprotein component of ND with respect to particle formation and stability. An 18-residue synthetic amphipathic a-helical peptide, termed 4F (Ac-D-W-F-K-A-F-Y-D-K-V-A-EK-F-K-E-A-F-NH2), solubilized vesicles comprised of egg phosphatidylcholine (egg PC), dipentadecanoyl PC or dimyristoylphosphatidylcholine (DMPC) at rates greater than or equal to solubilization rates observed with human apolipoprotein A-I (apoA-I; 243 amino acids). Characterization studies revealed that interaction with DMPC induced a near doubling of 4F tryptophan fluorescence emission quantum yield (excitation 280 nm) and a similar to 7 nm blue shift in emission wavelength maximum. inclusion of AMB in the vesicle substrate resulted in formation of 4F AMB-ND. Spectra of AMB containing particles revealed the antibiotic is a highly effective quencher of 4F tryptophan fluorescence emission, giving rise to a Ksv = 7.7 x 10(4). Negative stain electron microscopy revealed that AMB-ND prepared with 4F possessed a disk shaped morphology similar to ND prepared without AMB or prepared with apoA-I. In yeast and pathogenic fungi growth inhibition assays, 4F AMBND was as effective as apoA-I AMB-ND. The data indicate that AMB-ND generated using an amphipathic peptide in lieu of apoA-I form a discrete population of particles that possess potent biological activity. Given their intrinsic versatility, peptides may be preferred for scale up and clinical application of AMB-ND.

Impact Factor: 2.701 Cited Reference Count: 16

Void growth by dislocation-loop emission

Ahn, D. C., P. Sofronis, M. Kumar, J. Belak and R. Minich

Journal of Applied Physics **101**(6), 2007.

Experimental results from spall tests on aluminum reveal the presence of a dense dislocation structure in an annulus around a void that grew under the tensile pulse when a shock wave was reflected at the free surface of the specimen. The proposition is that dislocation emission from the void surface under load is a viable mechanism for void growth. To understand void growth in the absence of diffusive effects, the interstitial-loop emission mechanism under tensile hydrostatic stress is investigated. First, the micromechanics of pile-up formation when interstitial loops are emitted from a void under applied macroscopic loading is reviewed. Demand for surface energy expenditure upon void-surface change is taken into consideration. It is demonstrated that in face-centered cubic metals loop emission from voids with a radius of similar to 10 nm is indeed energetically possible in the hydrostatic stress environment generated by shock loading. On the other hand, the levels of hydrostatic stress prevalent in common structural applications are not sufficient to drive loops at equilibrium positions above a similar to 10 nm void. However, for voids larger than about 100 nm, the energetics of loop emission are easily met as a necessary condition even under the low stress environment prevalent in structural applications. (c) 2007 American Institute of Physics.

Impact Factor: 2.498 Cited Reference Count: 33

Radiation damage mechanisms for luminescence in Eu-doped GaN

Tringe, J. W., T. E. Felter, C. E. Talley, J. D. Morse, C. G. Stevens, J. M. Castelaz and C. Wetzel

Journal of Applied Physics **101**(5), 2007.

Thin films of Eu-doped GaN were irradiated with 500 keV He+ ions to understand radiation damage mechanisms and to quantify luminescence efficiency. The dependence of ion-beam-induced luminescence intensity on ion fluence was consistent with the simultaneous creation of nonradiative defects and the destruction of luminescent centers associated with 4f-4f core-level transitions in Eu3+. This model contrasts with a previous description which takes into account only nonradiative defect generation in GaN:Eu. Based on light from a BaF2 scintillator standard, the luminescent energy generation efficiency of GaN:Eu films doped to similar to 3x10(18) cm(-3) Eu is estimated to be similar to 0.1%. (c) 2007 American Institute of Physics.

Impact Factor: 2.498 Cited Reference Count: 18

Fragmentation in biaxial tension

Campbell, G. H., G. C. Archbold, O. A. Hurricane and P. L. Miller

Journal of Applied Physics **101**(3), 2007.

We have carried out an experiment that places a ductile stainless steel in a state of biaxial tension at a high rate of strain. The loading of the ductile metal spherical cap is performed by the detonation of a high-explosive layer with a conforming geometry to expand the metal radially outwards. Simulations of the loading and expansion of the metal predict strain rates that compare well with experimental observations. A high percentage of the high explosives loaded material was recovered through a soft capture process, and characterization of the recovered fragments provided high- quality data, including uniform strain prior to failure and fragment size. These data were used with a modified fragmentation model to determine a fragmentation energy. (c) 2007 American Institute of Physics.

Impact Factor: 2.498

Characterization of sputtering products during graphite exposure to deuterium ions by molecular dynamics

Marian, J., L. A. Zepeda-Ruiz, N. Couto, E. M. Bringa, G. H. Gilmer, P. C. Stangeby and T. D. Rognlien

Journal of Applied Physics **101**(4), 2007.

We study sputtering by 100 eV deuterium irradiation on deuterated amorphous carbon layers at 300 K using molecular dynamics (MD) simulations. Two main results are reported here. First, a special mechanism for carbon release-additional to and distinct from the standard definitions for physical and chemical sputtering of carbon by hydrogen isotopes-has been identified and quantified. This process, here termed ion induced release of unsaturated hydrocarbons (IRUH's), is primarily due to a recently identified atomic collision process where momentum from an impacting particle is transferred approximately perpendicular to the C-C bond, severing it. For the prescribed conditions, the IRUH yield has been found to be comparable to that of standard physical and chemical sputtering, the former being also consistently and simultaneously calculated here. IRUH release of single C atoms does not involve any hydrogenic chemistry and is therefore properly considered to be a distinct and additive type of physical sputtering to that of standard physical sputtering. For 100 eV D+ the single C yields of the two physical sputtering mechanisms have been found to be approximately equal. IRUH release of carbon is directly from the surface region of the solid and is separate from, and additional to, standard chemical sputtering (not included in these MD calculations), which typically produces saturated hydrocarbons such as CD4, from regions extending over the stopping depth of the deuteron in the solid. IRUH is evidently included in experimental measurements of total sputtering yield, e.g., by weight loss. The average energy of IRUH carbon products is about 1 eV and the angular distribution is consistent with a cosine distribution. Second, it is found that for the standard physically sputtered single C atoms the energy distribution is roughly consistent with the widely used Thompson distribution-this despite the fact that the assumptions on which the Thompson distribution is based are not satisfied for 100 eV D on C. The angular distribution of the standard physically sputtered single C atoms is also found to be consistent with the usually assumed cosine distribution.

Impact Factor: 2.498

Quantification of the size-dependent energy gap of individual CdSe quantum dots by valence electron energy-loss spectroscopy

Erni, R. and N. D. Browning

Ultramicroscopy **107**(2-3): 267-273, 2007.

Valence electron energy-loss spectroscopy (VEELS) performed in a monochromated scanning transmission electron microscope was used to measure the energy gaps of individual quantum dots (QDs). The gap energies of a series of CdSe QDs measured by VEELS reveal the expected quantum confinement effect; the gap energy increases with decreasing particle size. However, the values derived from these first VEELS measurements of single QDs are larger than the values commonly measured by optical spectroscopy. As standard optical methods lack the spatial resolution to probe individual nanoparticles, the particle-size distribution influences the optical response. It is suggested that the impact of the particle-size distribution accounts for the discrepancy between the energy-gap values derived from VEELS of single QDs and from optical methods of ensembles of QDs. Published by Elsevier B.V.

Impact Factor: 2.490 Cited Reference Count: 39

Practical considerations for high spatial and temporal resolution dynamic transmission electron microscopy

Armstrong, M. R., K. Boyden, N. D. Browning, G. H. Campbell, J. D. Colvin, W. J. DeHope, A. M. Frank, D. J. Gibson, F. Hartemann, J. S. Kim, W. E. King, T. B. LaGrange, B. J. Pyke, B. W. Reed, R. M. Shuttlesworth, B. C. Stuart and B. R. Torralva

Ultramicroscopy **107**(4-5): 356-367, 2007.

Although recent years have seen significant advances in the spatial resolution possible in the transmission electron microscope (TEM), the temporal resolution of most microscopes is limited to video rate at best. This lack of temporal resolution means that our understanding of dynamic processes in materials is extremely limited. High temporal resolution in the TEM can be achieved, however, by replacing the normal thermionic or field emission source with a photoemission source. In this case the temporal resolution is limited only by the ability to create a short pulse of photoexcited electrons in the source, and this can be as short as a few femtoseconds. The operation of the photoemission source and the control of the subsequent pulse of electrons (containing as many as 5 x 10(7) electrons) create significant challenges for a standard microscope column that is designed to operate with a single electron in the column at any one time. In this paper, the generation and control of electron pulses in the TEM to obtain a temporal resolution < 10(-6) S will be described and the effect of the pulse duration and current density on the spatial resolution of the instrument will be examined. The potential of these levels of temporal and spatial resolution for the study of dynamic materials processes will also be discussed.

Impact Factor: 2.490

Electrochemical impedance spectroscopy study of the passive films of alloy 22 in low pH nitrate and chloride environments

Gray, J. J. and C. A. Orme

Electrochimica Acta **52**(7): 2370-2375, 2007.

Utilizing electrochemical impedance spectroscopy (EIS), we characterize the passive film properties of alloy 22 during immersion in low pH nitrate and chloride solutions. In pure HCl, the passive film grows thinner with increasing acid concentration. In contrast, in HNO3, the passive film corrosion protection properties are enhanced, which leads to low corrosion rates, even at pH < -0.5. The combined influence of both HCl and HNO3 in contact simultaneously with the alloy 22 surface shows multiple phases in the passive film properties depending on the pH. EIS results show that the passive film changes either thickness and/or composition as the system is driven chemically through different corrosion states, including: active. passive, active/passive and transpassive. (c) 2006 Elsevier Ltd. All rights reserved.

Impact Factor: 2.453

Corrosion resistance of thermally sprayed high-boron iron-based amorphous-metal coatings: Fe49.7Cr17.7Mn1.9Mo7.4W1.6B15.2C3. 8Si2.4

Farmer, J. C., J. J. Haslam, S. D. Day, T. Lian, C. K. Saw, P. D. Hailey, J. S. Choi, R. B. Rebak, N. Yang, J. H. Payer, J. H. Perepezko, K. Hildal, E. J. Lavernia, L. Ajdelsztajn, D. J. Branagan, E. J. Buffa and L. F. Aprigliano

Journal of Materials Research **22**(8): 2297-2311, 2007.

An iron-based amorphous metal, Fe49.7Cr17.7Mn1.9Mo7.4W1.6B15.2C3.8Si2.4 (SAM2X5), with very good corrosion resistance has been developed, This material was prepared as a melt-spun ribbon, as well as gas atomized powder and a thermal-spray coating. During electrochemical testing in several environments, including seawater at 90 degrees C, the passive film stability was found to be comparable to that of high-performance nickel-based alloys and superior to that of stainless steels, based on electrochemical measurements of the passive film breakdown potential and general corrosion rates. This material also performed very well in standard salt fog tests. Chromium (Cr), molybdenum (Mo), and tungsten (W) provided corrosion resistance, and boron (B) enabled glass formation. The high boron content of this particular amorphous metal made it an effective neutron absorber and suitable for criticality control applications. This material and its parent alloy maintained corrosion resistance up to the glass transition temperature and remained in the amorphous state during exposure to relatively high neutron doses.

Impact Factor: 2.354 Cited Reference Count: 35

The effects of tensile plastic deformation on the hardness and Young's modulus of a bulk nanocrystalline alloy studied by nanoindentation

Fan, G. J., W. H. Jiang, F. X. Liu, H. Choo, P. K. Liaw, B. Yang, L. F. Fu and N. D. Browning

Journal of Materials Research **22**(5): 1235-1239, 2007.

A bulk nanocrystalline (nc) Ni-Fe alloy was subjected to tensile deformation, which leads to grain growth. The nanoindentation study indicates that the hardness, H, and Young's modulus, E, of the nc alloy before and after tensile deformation did not show a clear indentation-rate effect. However, the tensile deformation results in a decrease in the E values of about 15%, which might be attributed to the grain rotation, leading to texture development during the stress-induced grain growth.

Impact Factor: 2.354 Cited Reference Count: 32

Thermodynamics of mono- and di-vacancies in barium titanate

Erhart, P. and K. Albe

Journal of Applied Physics **102**(8): 8, 2007.

The thermodynamic and kinetic properties of mono- and di-vacancy defects in cubic (para-electric) barium titanate BaTiO3 are studied by means of density-functional theory calculations. It is determined which vacancy types prevail for given thermodynamic boundary conditions. The calculations confirm the established picture that vacancies occur in their nominal charge states almost over the entire band gap. For the dominating range of the band gap the di-vacancy binding energies are constant and negative. The system, therefore, strives to achieve a state in which, under metal-rich (oxygen-rich) conditions, all metal (oxygen) vacancies are bound in di-vacancy clusters. The migration barriers are calculated for mono-vacancies in different charge states. As oxygen vacancies are found to readily migrate at typical growth temperatures, di-vacancies can be formed at ease. The key results of the present study with respect to the thermodynamic behavior of mono- and di-vacancies influence the initial defect distribution in the ferroelectric phases and therefore the conditions for aging.

Impact Factor: 2.316 Cited Reference Count: 70

Effect of the density of collision cascades on ion implantation damage in ZnO

Azarov, A. Y., S. O. Kucheyev, A. I. Titov and P. A. Karaseov

Journal of Applied Physics **102**(8): 5, 2007.

We study structural disorder in ZnO bombarded at room temperature with 1.3 keV/amu atomic P and cluster PFn (n=2 and 4) ions. Rutherford backscattering/channeling spectrometry results show that the density of collision cascades has a negligible effect on the damage buildup in the crystal bulk in the dose range resulting in similar to 1.5-15 displacements per atom. Hence, the amount of stable post-implantation disorder in the bulk can be predicted based on ballistic calculations. In contrast, the cascade density affects radiation damage in the near-surface region. An intermediate defect peak between the expected surface and bulk peaks of disorder forms for ion irradiation conditions with dense cascades.

Impact Factor: 2.316 Cited Reference Count: 14

Electronic structure of chromia aerogels from soft x-ray absorption spectroscopy

Kucheyev, S. O., B. Sadigh, T. F. Baumann, Y. M. Wang, T. E. Felter, T. van Buuren, A. E. Gash, J. H. Satcher and A. V. Hamza

Journal of Applied Physics **101**(12): 8, 2007.

The electronic structure of ultralow density nanoporous chromia monoliths (aerogels) is studied by soft x-ray absorption near-edge structure (XANES) spectroscopy. These aerogels are prepared by the epoxide sol-gel method. High-resolution O K edge and Cr L-2,L-3 edge XANES spectra of aerogels (before and after thermal annealing at 550 degrees C) are compared with spectra of microcrystalline alpha-Cr2O3 and orthorhombic CrO3 powders, alpha-Cr2O3 (0001) and (1102) single crystals, and an unrelaxed amorphous phase of full-density Cr2O3. Spectra are interpreted based on the results of crystal-field multiplet calculations (for Cr L-2,L-3 edge) and ab initio spin-polarized density functional theory calculations with and without a Hubbard-type on-site Coulomb repulsion (for O K edge). Results show that the electronic structure of as-prepared aerogels, with a large fraction of undercoordinated surface atoms, is significantly different from that of bulk alpha-Cr2O3, CrO3, or amorphous Cr2O3. Thermal treatment transforms the as-prepared amorphous aerogel into alpha-Cr2O3 nanopowder.

Impact Factor: 2.316 Cited Reference Count: 47

Microstructure morphology of shock-induced melt and rapid resolidification in bismuth

Colvin, J. D., B. W. Reed, A. F. Jankowski, M. Kumar, D. L. Paisley, D. C. Swift, T. E. Tierney and A. M. Frank

Journal of Applied Physics **101**(8), 2007.

With the growing importance of nanotechnology, there is increased emphasis on rapid solidification processing to produce materials microstructures with a finer length scale. However, few studies have focused on the question of how a material restructures itself on the microstructural scale when it refreezes at very high cooling rates. Here we report on the development of microstructures in pure bismuth metal as it is subjected to rapid shock-driven melting and subsequent resolidification (on release of pressure), where the estimated effective undercooling rates are on the order of 10(10) K/s, orders of magnitude faster than any achieved before in bulk material. Microscopic examination of the recovered material indicates that the melting transformation was far from homogeneous, and substantial morphological changes are observed compared to the starting microstructure. (c) 2007 American Institute of Physics.

Impact Factor: 2.316 Cited Reference Count: 39

Proof of principle experiments that demonstrate utility of cocktail hohlraums for indirect drive ignition

Jones, O. S., J. Schein, M. D. Rosen, L. J. Suter, R. J. Wallace, E. L. Dewald, S. H. Glenzer, K. M. Campbell, J. Gunther, B. A. Hammel, O. L. Landen, C. M. Sorce, R. E. Olson, G. A. Rochau, H. L. Wilkens, J. L. Kaae, J. D. Kilkenny, A. Nikroo and S. P. Regan

Physics of Plasmas **14**(5): 11, 2007.

This work is a summary of experiments, numerical simulations, and analytic modeling that demonstrate improved radiation confinement when changing from a hohlraum made from gold to one made from a mixture of high Z materials ("cocktail"). First, the results from several previous planar sample experiments are described that demonstrated the potential of cocktail wall materials. Then a series of more recent experiments are described in which the radiation temperatures of hohlraums made from uranium-based cocktails were directly measured and compared with a gold reference hohlraum. Cocktail hohlraums meeting the oxygen specification (< 5% atomic fraction oxygen) demonstrated an increase in radiation of up to 7 eV, agreeing well with modeling. When applied to an indirectly driven fusion capsule absorbing -160 kJ of x-ray energy, these data suggest that a hohlraum made from a suitably chosen uranium-based cocktail would have about 17% less wall losses and require about 10% less laser energy than a gold hohlraum of the same size.

Impact Factor: 2.258 Cited Reference Count: 20

Very-high-growth-factor planar ablative Rayleigh-Taylor experiments

Bradley, D. K., D. G. Braun, S. G. Glendinning, M. J. Edwards, J. L. Milovich, C. M. Sorce, G. W. Collins, S. W. Haan, R. H. Page, R. J. Wallace and J. L. Kaae

Physics of Plasmas **14**(5): 7, 2007.

The Rayleigh-Taylor (RT) instability is an important factor in bounding the performance envelope of inertial confinement fusion targets. This paper describes an experiment for ablative RT instability that for the first time achieves growth factors close to those expected to occur in indirect-drive ignition targets at the National Ignition Facility (NIF) [J. A. Paisner, J. D. Boyes, S. A. Kumpan et al., Laser Focus World 30, 75 (1994)]. The large growth allows small-seed perturbations to be detected and can be used to place an upper bound on perturbation growth at the ablation front resulting from microstructure or surface roughness in the preferred Be ablator. The experiments were performed on the Omega laser [T. R. Boehly, D. L. Brown, R. S. Craxton et al., Optics Communications 133, 495 (1997)] using a two stepped x-ray pulse consisting of an early time section to emulate the NIF foot followed by a higher-radiation-temperature drive sustained over an additional 5-7 ns. The trajectory of the ablator was measured using streaked backlit radiography, and the growth of a sinusoidal perturbation machined on the drive side of the ablator was measured using face-on radiography. The diagnostic view remained open until -11 ns with maximum growth factors measured to be -200.

Impact Factor: 2.258 Cited Reference Count: 26

Very-high-growth-factor planar ablative Rayleigh-Taylor experiments

Bradley, D. K., D. G. Braun, S. G. Glendinning, M. J. Edwards, J. L. Milovich, C. M. Sorce, G. W. Collins, S. W. Haan, R. H. Page, R. J. Wallace and J. L. Kaae

Physics of Plasmas **14**(5): 56313-56313, 2007.

The Rayleigh-Taylor (RT) instability is an important factor in bounding the performance envelope of inertial confinement fusion targets. This paper describes an experiment for ablative RT instability that for the first time achieves growth factors close to those expected to occur in indirect-drive ignition targets at the National Ignition Facility (NIF) [J. A. Paisner, J. D. Boyes, S. A. Kumpan et al., Laser Focus World 30, 75 (1994)]. The large growth allows small-seed perturbations to be detected and can be used to place an upper bound on perturbation growth at the ablation front resulting from microstructure or surface roughness in the preferred Be ablator. The experiments were performed on the Omega laser [T. R. Boehly, D. L. Brown, R. S. Craxton et al., Optics Communications 133, 495 (1997)] using a two stepped x-ray pulse consisting of an early time section to emulate the NIF foot followed by a higher-radiation-temperature drive sustained over an additional 5-7 ns. The trajectory of the ablator was measured using streaked backlit radiography, and the growth of a sinusoidal perturbation machined on the drive side of the ablator was measured using face-on radiography. The diagnostic view remained open until -11 ns with maximum growth factors measured to be -200. (C) 2007 American Institute of Physics.

Impact Factor: 2.258

Proof of principle experiments that demonstrate utility of cocktail hohlraums for indirect drive ignition

Jones, O. S., J. Schein, M. D. Rosen, L. J. Suter, R. J. Wallace, E. L. Dewald, S. H. Glenzer, K. M. Campbell, J. Gunther, B. A. Hammel, O. L. Landen, C. M. Sorce, R. E. Olson, G. A. Rochau, H. L. Wilkens, J. L. Kaae, J. D. Kilkenny, A. Nikroo and S. P. Regan

Physics of Plasmas **14**(5): 56311-56311, 2007.

This work is a summary of experiments, numerical simulations, and analytic modeling that demonstrate improved radiation confinement when changing from a hohlraum made from gold to one made from a mixture of high Z materials (“cocktail”). First, the results from several previous planar sample experiments are described that demonstrated the potential of cocktail wall materials. Then a series of more recent experiments are described in which the radiation temperatures of hohlraums made from uranium-based cocktails were directly measured and compared with a gold reference hohlraum. Cocktail hohlraums meeting the oxygen specification (< 5% atomic fraction oxygen) demonstrated an increase in radiation of up to 7 eV, agreeing well with modeling. When applied to an indirectly driven fusion capsule absorbing -160 kJ of x-ray energy, these data suggest that a hohlraum made from a suitably chosen uranium-based cocktail would have about 17% less wall losses and require about 10% less laser energy than a gold hohlraum of the same size. (C) 2007 American Institute of Physics.

Impact Factor: 2.258

Analytical scanning and transmission electron microscopy of laboratory impacts on Stardust aluminum foils: Interpreting impact crater morphology and the composition of impact residues

Kearsley, A. T., G. A. Graham, M. J. Burchell, M. J. Cole, Z. R. Dai, N. Teslich, J. P. Bradley, R. Chater, P. A. Wozniakiewicz, J. Spratt and G. Jones

Meteoritics & Planetary Science **42**(2): 191-210, 2007.

The known encounter velocity (6.1 kms(-1)) and particle incidence angle (perpendicular) between the Starchist spacecraft and the dust emanating from the nucleus of comet Wild-2 fall within a range that allows simulation in laboratory light-gas gun (LGG) experiments designed to validate analytical methods for the interpretation of dust impacts on the aluminum foil components of the Stardust collector. Buckshot of a wide size, shape, and density range of mineral, glass, polymer, and metal grains, have been fired to impact perpendicularly on samples of Stardust Al 1100 foil, tightly wrapped onto aluminum alloy plate as an analogue of foil on the spacecraft collector. We have not yet been able to produce laboratory impacts by projectiles with weak and porous aggregate structure, as may occur in some cometary dust grains. In this report we present information on crater gross morphology and its dependence on particle size and density, the pre-existing major- and trace-element composition of the foil, geometrical issues for energy dispersive X-ray analysis of the impact residues in scanning electron microscopes, and the modification of dust chemical composition during creation of impact craters as revealed by analytical transmission electron microscopy. Together, these observations help to underpin the interpretation of size, density, and composition for particles impacted on the Stardust aluminum foils.

Impact Factor: 2.253

Compaction behavior of uniaxially cold-pressed Bi-Ta composites

Martin, L. P., A. M. Hodge and G. H. Campbell

Scripta Materialia **57**(3): 229-232, 2007.

Compaction of Bi and Ta powders was performed by uniaxial pressing at room temperature. Post-pressing density was evaluated as a function of the compaction pressure, and indicated that as the Ta content increases there is a reduction in density for comparable pressing conditions. A modified Heckel equation is used to evaluate the compaction behavior. The analysis indicates that the yield pressure increases with increasing Ta content while the Poisson's ratio is not significantly affected. The yield pressure derived from the analysis compares favorably with published compression testing data for polycrystalline Bi.

Impact Factor: 2.161 Cited Reference Count: 25

Strength and thermal stability of nanocrystalline gold alloys

Wang, Y. M., A. F. Jankowski and A. V. Hamza

Scripta Materialia **57**(4): 301-304, 2007.

By additions of Cu and Sn elements, we have synthesized nanocrystalline Au-Cu and Au-Cu-Sn materials with a minimum grain size down to similar to 3 nm. Tensile measurements of these nanocrystalline materials indicate that the Hall-Petch scaling law is maintained to the smallest length scale. Though Cu and Sn solid solutions are observed to have little effect on the strength of nanocrystalline An, they substantially enhance the thermal stability of these alloys. Abnormal grain growth no longer becomes the characteristic feature of alloyed nanocrystalline Au.

Impact Factor: 2.161 Cited Reference Count: 21

2nd TMS Symposium on biological materials science

Hodge, A. M., M. A. Meyers, C. T. Lim and R. LeSar

Acta Biomaterialia 3(3): 287-288, 2007.

Impact Factor: 2.132

Heat transfer and fluid flow during keyhole mode laser welding of tantalum, Ti-6Al-4V, 304L stainless steel and vanadium

Rai, R., J. W. Elmer, T. A. Palmer and T. DebRoy

Journal of Physics D-Applied Physics **40**(18): 5753-5766, 2007.

Because of the complexity of several simultaneous physical processes, most heat transfer models of keyhole mode laser welding require some simplifications to make the calculations tractable. The simplifications often limit the applicability of each model to the specific materials systems for which the model is developed. In this work, a rigorous, yet computationally efficient, keyhole model is developed and tested on tantalum, Ti-6Al-4V,304L stainless steel and vanadium. Unlike previous models, this one combines an existing model to calculate keyhole shape and size with numerical fluid flow and heat transfer calculations in the weld pool. The calculations of the keyhole profile involved a point-by-point heat balance at the keyhole walls considering multiple reflections of the laser beam in the vapour cavity. The equations of conservation of mass, momentum and energy are then solved in three dimensions assuming that the temperatures at the keyhole wall reach the boiling point of the different metals or alloys. A turbulence model based on Prandtl's mixing length hypothesis was used to estimate the effective viscosity and thermal conductivity in the liquid region. The calculated weld cross-sections agreed well with the experimental results for each metal and alloy system examined here. In each case, the weld pool geometry was affected by the thermal diffusivity, absorption coefficient, and the melting and boiling points, among the various physical properties of the alloy. The model was also used to better understand solidification phenomena and calculate the solidification parameters at the trailing edge of the weld pool. These calculations indicate that the solidification structure became less dendritic and coarser with decreasing weld velocities over the range of speeds investigated in this study. Overall, the keyhole weld model provides satisfactory simulations of the weld geometries and solidification sub-structures for diverse engineering metals and alloys.

Impact Factor: 2.077

Spin resolved photoelectron spectroscopy of Fe3O4: the case against half-metallicity

Tobin, J. G., S. A. Morton, S. W. Yu, G. D. Waddill, I. K. Schuller and S. A. Chambers

Journal of Physics-Condensed Matter **19**(31): 15218-15218, 2007.

Many materials have been theoretically predicted to be half-metallic, and hence suitable for use as pure spin sources in spintronic devices. Yet to date, remarkably few of these predictions have been experimentally verified. We have used spin polarized photoelectron spectroscopy to study one candidate half-metallic system, Fe3O4. Such experiments are normally hampered by difficulties in producing clean stoichiometric surfaces with a polarization that is truly representative of that of the bulk. However, by utilizing higher photon energies than have traditionally been used for such experiments, we can study polarization in 'as received' samples, essentially 'looking through' the disrupted surface. High quality, strain relieved, ex situ prepared Fe3O4 films have been thoroughly characterized by diffraction, transport and magnetometry studies of their crystallographic, electronic and magnetic properties. The spectroscopic results are found to agree fairly closely with previously published experimental data on in situ grown thin films and cleaved single crystals. However, despite the higher photoelectron kinetic energies of the experiment, it has not been possible to observe 100% polarization at the Fermi level. Hence, our data do not support the claim of true half-metallicity for Fe3O4.

Impact Factor: 2.038

The first target experiments on the national ignition facility

Landen, O. L., S. H. Glenzer, D. H. Froula, E. L. Dewald, L. J. Suter, M. B. Schneider, D. E. Hinkel, J. C. Fernandez, J. L. Kline, S. R. Goldman, D. G. Braun, P. M. Celliers, S. J. Moon, H. S. Robey, N. E. Lanier, S. G. Glendinning, B. E. Blue, B. H. Wilde, O. S. Jones, J. Schein, L. Divol, D. H. Kalantar, K. M. Campbell, J. P. Holder, J. W. McDonald, C. Niemann, A. J. Mackinnon, G. W. Collins, D. K. Bradley, J. H. Eggert, D. C. Hicks, G. Gregori, R. K. Kirkwood, B. K. Young, J. M. Foster, J. F. Hansen, T. S. Perry, D. H. Munro, H. A. Baldis, G. P. Grim, R. F. Heeter, M. B. Hegelich, D. S. Montgomery, G. A. Rochau, R. E. Olson, R. E. Turner, J. B. Workman, R. L. Berger, B. I. Cohen, W. L. Kruer, A. B. Langdon, S. H. Langer, N. B. Meezan, H. A. Rose, C. H. Still, E. A. Williams, E. S. Dodd, M. J. Edwards, M. C. Monteil, R. M. Stevenson, B. R. Thomas, R. F. Coker, C. R. Magelssen, P. A. Rosen, P. E. Stry, D. Woods, S. V. Weber, P. E. Young, S. Alvarez, G. Armstrong, R. Bahr, J. L. Bourgade, D. Bower, J. Celeste, M. Chrisp, S. Compton, J. Cox, C. Constantin, R. Costa, J. Duncan, A. Ellis, J. Emig, C. Gautier, A. Greenwood, R. Griffith, F. Holdner, G. Holtmeier, D. Hargrove, T. James, J. Kamperschroer, J. Kimbrough, M. Landon, F. D. Lee, R. Malone, M. May, S. Montelongo, J. Moody, E. Ng, A. Nikitin, D. Pellinen, K. Piston, M. Poole, V. Rekow, M. Rhodes, R. Shepherd, S. Shiromizu, D. Voloshin, A. Warrick, P. Watts, F. Weber, P. Young, P. Arnold, L. Atherton, G. Bardsley, R. Bonanno, T. Borger, M. Bowers, R. Bryant, S. Buckman, S. Burkhart, F. Cooper, S. N. Dixit, G. Erbert, D. C. Eder, R. E. Ehrlich, B. Felker, J. Fornes, G. Frieders, S. Gardner, C. Gates, M. Gonzalez, S. Grace, T. Hall, C. A. Haynam, J. Neumann, A. Newton, P. Opsahl, E. Padilla, T. Parham, G. Parrish, C. Petty, M. Polk, C. Powell, I. Reinbachs, R. Rinnert, B. Riordan, G. Ross, V. Robert, M. Tobin, S. Sailors, R. Saunders, M. Schmitt, M. Shaw, M. Singh, M. Spaeth, A. Stephens, G. Tietbohl, J. Tuck, B. M. Van Wonterghem, R. Vidal, P. J. Wegner, P. Whitman, K. Williams, K. Winward, K. Work, R. Wallace, A. Nobile, M. Bono, B. Day, J. Elliott, D. Hatch, H. Louis, R. Manzenares, D. O'Brien, P. Papin, T. Pierce, G. Rivera, J. Ruppe, D. Sandoval, D. Schmidt, L. Valdez, K. Zapata, B. J. MacGowan, M. J. Eckart, W. W. Hsing, P. T. Springer, B. A. Hammel, E. I. Moses and G. H. Miller

European Physical Journal D **44**(2): 273-281, 2007.

A first set of shock timing, laser-plasma interaction, hohlraum energetics and hydrodynamic experiments have been performed using the first 4 beams of the National Ignition Facility (NIF), in support of indirect drive Inertial Confinement Fusion (ICF) and High Energy Density Physics (HEDP). In parallel, a robust set of optical and X-ray spectrometers, interferometer, calorimeters and imagers have been activated. The experiments have been undertaken with laser powers and energies of up to 8 TW and 17 kJ in flattop and shaped 1-9 ns pulses focused with various beam smoothing options. The experiments have demonstrated excellent agreement between measured and predicted laser-target coupling in foils and hohlraums, even when extended to a longer pulse regime unattainable at previous laser facilities, validated the predicted effects of beam smoothing oil intense laser beam propagation in long scale-length plasmas and begun to test 3D codes by extending the study of laser driven hydrodynamic jets to 3D geometries.

Impact Factor: 1.988 Cited Reference Count: 61

Interface and defect structures in YBa2Cu3O7-delta and Nb : SrTiO3 heterojunction

Fu, L. F., N. D. Browning, W. Ramadan, S. B. Ogale, D. C. Kundaliya and T. Venkatesan

Journal of Physics D-Applied Physics **40**(1): 187-191, 2007.

YBa2Cu3O7-delta thin films grown on a Nb-doped SrTiO3 substrate by a pulsed laser deposition method have been fully characterized by scanning transmission electron microscopy Z- contrast imaging and electron energy loss spectroscopy techniques. The Nb distribution was found to be uniform and unchanged across the interface, ensuring a high quality p - n junction heterointerface. We first observed the coexistence of 124 and 125 YBCO defect structure phases, appearing as planar defects in a YBCO thin film. Dispersive Y2O3 nanoparticles have also been observed in the thin film. The interaction of these defect structures and Y2O3 nanoparticles is thought to be beneficial for pinning flux through the entire film thickness.

Impact Factor: 1.957 Cited Reference Count: 22

Observation of an underlying relativistic effect in the valence bands of Pt

Yu, S. W. and J. G. Tobin

Surface Science **601**(23): L127-L131, 2007.

We have measured the photoelectron spin polarization emitted by unpolarized UV radiation from the valence-bands of the well ordered Pt(001)-(5 x 1) surface and the disordered surface destroyed by Ar ions bombardment. Almost identical spin polarizations have been observed in both cases. This observation suggests that the electron spin polarization in photoemission caused by unpolarized light is determined by a short-range order of atoms. This finding has an obvious implication that the electron spin polarization in photoemission caused by unpolarized light can be used to study the bulk electronic structure of the nonmagnetic materials.

Impact Factor: 1.880 Cited Reference Count: 27

Sulfur-induced mobilization of Au surface atoms on Au(111) studied by real-time STM

Biener, M. M., J. Biener and C. M. Friend

Surface Science **601**(7): 1659-1667, 2007.

The interaction of sulfur with gold surfaces has attracted considerable interest due to numerous technological applications such as the formation of self-assembled monolayers and as a chemical sensor. Here, we report on the interaction of sulfur with Au(1 1 1) at two different temperatures (300 K and 420 K) studied by real-time scanning tunnelling microscopy, low energy electron diffraction and Auger electron spectroscopy. In the low coverage regime (< 0.1 ML), S adsorption lifts the herringbone reconstruction of the clean Au(1 1 1) surface indicating a lateral expansion of the surface layer. An ordered (root 3 x root 3)R30 degrees sulfur adlayer develops as the coverage reaches similar to 0.3 ML. At higher S coverages (> 0.3 ML) gold surface atoms are removed from regular terrace sites and incorporated into a growing gold sulfide phase. At 300 K this process leads to the formation of a rough pit and mound surface morphology. This gold sulfide exhibits short-range order and an incommensurate, long-range ordered AuS phase develops upon annealing at 450-525 K. In contrast, formation of an ordered AuS phase via rapid step-retraction rather than etch pit formation is observed during S-interaction with Au(1 1 1) surfaces at 420 K. Our results shed new light on the S-Au(1 1 1) interaction.

Impact Factor: 1.880 Cited Reference Count: 38

Structure and catalytic activity of POSS-stabilized Pd nanoparticles

Letant, S. E., J. Herberg, L. N. Dinh, R. S. Maxwell, R. L. Simpson and A. P. Saab

Catalysis Communications **8**(12): 2137-2142, 2007.

Palladium nanoparticles stabilized with polyhedral oligomeric silsesquioxanes have been characterized and determined to function as a heterogeneous catalyst. TEM and SEM studies indicate the material comprises 2-5 nm diameter Pd crystallites in a POSS layer, which aggregate to form spherical secondary structures of about 50 nm in diameter. Solid-state NMR reveals that the primary interaction between Pd and POSS is through the alkyl-amino functional groups on the POSS cage, in addition to some weak interactions with the cage itself. This material is observed by microbalance measurements to efficiently catalyze the direct hydrogenation of 1,4-diphenylbutadiyne.

Impact Factor: 1.878 Cited Reference Count: 20

Topologically clean distance fields

Gyulassy, A. G., M. A. Duchaineau, V. Natarajan, V. Pascucci, E. M. Bringa, A. Higginbotham and B. Hamann

IEEE Transactions on Visualization and Computer Graphics **13**(6): 1432-1439, 2007.

Analysis of the results obtained from material simulations is important in the physical sciences. Our research was motivated by the need to investigate the properties of a simulated porous solid as it is hit by a projectile. This paper describes two techniques for the generation of distance fields containing a minimal number of topological features, and we use them to identify features of the material. We focus on distance fields defined on a volumetric domain considering the distance to a given surface embedded within the domain. Topological features of the field are characterized by its critical points. Our first method begins with a distance field that is computed using a standard approach, and simplifies this field using ideas from Morse theory. We present a procedure for identifying and extracting a feature set through analysis of the MS complex, and apply it to find the invariants in the clean distance field. Our second method proceeds by advancing a front, beginning at the surface, and locally controlling the creation of new critical points. We demonstrate the value of topologically clean distance fields for the analysis of filament structures in porous solids. Our methods produce a curved skeleton representation of the filaments that helps material scientists to perform a detailed qualitative and quantitative analysis of pores, and hence infer important material properties. Furthermore, we provide a set of criteria for finding the "difference" between two skeletal structures, and use this to examine how the structure of the porous solid changes over several timesteps in the simulation of the particle impact.

Impact Factor: 1.794 Cited Reference Count: 31

Substrate creep on the fatigue life of a model dental multilayer structure

Zhou, J., M. Huang, X. Niu and W. O. Soboyejo

Journal of Biomedical Materials Research Part B-Applied Biomaterials **82**B(2): 374-382, 2007.

In this article, we investigated the effects of substrate creep on the fatigue life of a model dental multilayer structure, in which a top glass layer was bonded to a polycarbonate substrate through a dental adhesive. The top glass layers were ground using 120 or 600 grit sand papers before bonding to create different subsurface crack sizes and morphologies. The multilayer structures were tested under cyclic Hertzian contact loading to study crack growth and obtain fatigue life curves. The experiment results showed that the fatigue lives of the multilayer structures were impaired by increasing crack sizes in the subsurfaces. They were also significantly reduced by the substrate creep when tested at relatively low load levels, i.e. P-m < 60 N (P-m is the maximum magnitude of cyclic load). But at relatively high load levels, i.e. P-m > 65 N,slow crack growth was the major failure mechanism. A modeling study was then carried out to explore the possible failure mechanisms over a range of load levels. It is found that fatigue life at relatively low load levels can be better estimated by considering the substrate creep effect. (C) 2007 Wiley Periodicals, Inc.

Impact Factor: 1.778 Cited Reference Count: 20

Sub-diffraction-limited multilayer coatings for the 0.3 numerical aperture micro-exposure tool for extreme ultraviolet lithography

Soufli, R., R. M. Hudyma, E. Spiller, E. M. Gullikson, M. A. Schmidt, J. C. Robinson, S. L. Baker, C. C. Walton and J. S. Taylor

Applied Optics **46**(18): 3736-3746, 2007.

Multilayer coating results are discussed for the primary and secondary mirrors of the micro-exposure tool (MET): a 0.30 NA lithographic imaging system with a 200 mu m X 600 mu m field of view at the wafer plane, operating in the extreme ultraviolet (EUV) region at an illumination wavelength around 13.4 nm. Mo/Si multilayers were deposited by DC-magnetron sputtering on large-area, curved MET camera substrates. A velocity modulation technique was implemented to consistently achieve multilayer thickness profiles with added figure errors below 0.1 nm rms demonstrating sub-diffraction-limited performance, as defined by the classical diffraction limit of Rayleigh (0.25 waves peak to valley) or Marechal (0.07 waves rms). This work is an experimental demonstration of sub-diffraction-limited multilayer coatings for high-NA EUV imaging systems, which resulted in the highest resolution microfield EUV images to date. (c) 2007 Optical Society of America.

Impact Factor: 1.717 Cited Reference Count: 21

Accurate labeling of the light-actinide O-4,O-5 edges

Moore, K. T. and G. van der Laan

Ultramicroscopy **107**(12): 1201-1206, 2007.

In this short article, the accurate labeling of the O-4,O-5 edges of the light actinides is addressed. The O-4 and O-5 edges are both contained in what is termed the 'giant resonance' and the smaller 'pre-peak' that is observed is a consequence of first-order perturbation by the 5d spin-orbit interaction on the 5d,5f exchange splitting. Thus, the small pre-peak in the actinide 5d --> 5f transition should not be labeled the OS peak, but rather the Delta S = 1 peak.

Impact Factor: 1.706

Characterization of ruthenium thin films as capping layer for extreme ultraviolet lithography mask blanks

Yan, P. Y., E. Spiller and P. Mirkarimi

Journal of Vacuum Science & Technology B **25**(6): 1859-1866, 2007.

In extreme ultraviolet lithography (EUVL), the multilayer (ML) damage-free mask patterning processes and damage-free usage cycle are the keys in obtaining a successful, functional EUVL mask. A robust ML capping layer design will enable a long mask lifetime. In this article detailed investigation on the viability of ruthenium (Ru) thin films as capping layer for EUVL ML mask blanks is presented. The study is focused on Ru capping layer design for high reflectivity and its properties relevant to EUVL mask applications, such as microstructure, stress, optical properties at EUV wavelength, and chemical durability. The authors found that Ru thin films with a crystalline structure present a very high compressive stress which is insensitive to the primary ion deposition source energy. The Ru/Si interdiffusion layer, however, presents a much lower stress than the of Ru-only film. Amorphization of the Ru film is via atomic composition modification, which the authors believe could be one of the keys in reducing Ru film stress. The ruthenium cap, under a piranha chemical clean, was found to be more durable than Si capped ML blanks, indicating the advantages of using Ru as the EUVL ML mask blank capping layer.

Impact Factor: 1.597 Cited Reference Count: 15

Growth and printability of multilayer phase defects on extreme ultraviolet mask blanks

Liang, T., E. Ultanir, G. Zhang, S. J. Park, E. Anderson, E. Gullikson, P. Naulleau, F. Salmassi, P. Mirkarimi, E. Spiller and S. Baker

Journal of Vacuum Science & Technology B **25**(6): 2098-2103, 2007.

The ability to fabricate defect-free reflective Mo-Si multilayer (ML) blanks is a well-recognized challenge in enabling extreme ultraviolet (EUV) lithography for semiconductor manufacturing. Both the specification and reduction of defects necessitate the understanding of their printability and how they are generated and grow during ML deposition. A ML phase defect can be depicted by its topographical profile on the surface as either a bump or pit, which is then characterized by height or depth and width. These phase defects are complex in nature and their impact to resist printing. The authors developed an effective way to study phase defects with programmed defect mask (PDM) as "model" test vehicle. The defects are produced with tuned ML deposition process and placed in varying proximity to absorber patterns on the mask. This article describes the recent study of ML phase defect printability from exposures of a ML PDM on the EUV microexposure tool with annular, monopole, and dipole illuminations. (c) 2007 American Vacuum Society.

Impact Factor: 1.597 Cited Reference Count: 13

Thermal stability and mechanical behavior of ultra-fine bcc Ta and V coatings

Jankowski, A. F., J. Go and J. P. Hayes

Surface & Coatings Technology **202**(4-7): 957-961, 2007.

Ultra-refined microstructures of both tantalum (Ta) and vanadium (V) are produced using electron-beam evaporation and magnetron sputtering deposition. The thermal stability of the micron-to-submicron grain size foils is examined to quantify the kinetics and activation energy of diffusion, as well as identify the temperature transition in dominant mechanism from grain boundary to lattice diffusion. The activation energies for boundary diffusion in Ta and V determined from grain growth are 0.3 and 0.2 eV atom(-1), respectively, versus lattice diffusion values of 4.3 and 3.2 eV atom(-1), respectively. The mechanical behavior, as characterized by strength and hardness, is found to inversely scale with square-root grain size according to the Hall-Petch relationship. The strength of Ta and V increases two-fold from 400 MPa, as the grain size decreases from 2 to 0.75 mu m.

Impact Factor: 1.559 Cited Reference Count: 26

Semi-empirical modeling of the sputter deposition of coatings onto spherical capsules

Jankowski, A. F. and J. P. Hayes

Surface & Coatings Technology **202**(4-7): 904-909, 2007.

The sputter deposition of coatings onto spherical capsules is accomplished using a chambered substrate platform. Oxides and metal coatings are sputter deposited through a screen-aperture array onto a 0.3-1.2 mm diameter, solid spheres and hollow shells. Each capsule is individually chambered within a larger array. Ultrasonic vibration is used to produce a random bounce of each chambered capsule in order to produce a coating with uniform thickness. Characterization of aluminum-oxide coated, platinum solid spheres and copper-gold layer coated, hollow capsules indicate that uniform coatings can be produced using a screen-apertured chamber as the substrate platform. Potential advantages of this approach compared to open-bounce pans include improved sample yield and reduced surface roughness since exposure to debris is minimized. A semiempirical process model for the coating growth on the capsules is developed to assess selection of the screen aperture based on the sputtering parameters and the coating materials.

Impact Factor: 1.559 Cited Reference Count: 8

Nanosecond x-Ray diffraction from polycrystalline and amorphous materials in a pinhole camera geometry suitable for laser shock compression experiments

Hawreliak, J., H. E. Lorenzana, B. A. Remington, S. Lukezic and J. S. Wark

Review of Scientific Instruments **78**(8): 6, 2007.

Nanosecond pulses of quasimonochromatic x-rays emitted from the K shell of ions within a laser-produced plasma are of sufficient spectral brightness to allow single-shot recording of powder diffraction patterns from thin foils of order millimeter diameter. Strong diffraction signals have been observed in a cylindrical pinhole camera arrangement from both polycrystalline and amorphous foils, and the experimental arrangement and foil dimensions are such that they allow for laser shocking or quasi-isentropic loading of the foil during the diffraction process.

Impact Factor: 1.541 Cited Reference Count: 30

ToF-SIMS characterization of uranium hydride

Morrall, P., D. W. Price, A. J. Nelson, W. J. Siekhaus, E. Nelson, K. J. Wu, M. Stratman and W. McLean

Philosophical Magazine Letters **87**(8): 541-547, 2007.

Time-of-flight secondary-ion mass spectrometry (ToF-SIMS) has been employed for the first time to investigate uranium hydride. The deuterated form of uranium hydride (UD3) was formed on a polycrystalline uranium sample by exposure to high-purity D-2 gas at room temperature. The characteristic positive and negative secondary-ion fragments observed from uranium hydride are reported and assigned. Our investigations show that negative-ion fragments provide the most unambiguous method for identification of uranium hydride, through the detection of UH2- and UH4- fragments. In addition, density functional theory (DFT) calculations are presented which confirm the identity and stability of, and also assign structural geometries to, the ion fragments observed within the SIMS experiment. The DFT calculations show that UH2+/- ions adopt a linear arrangement, whereas positive tri- and tetrahydride ions (UH3+, UH4+) adopt structures based on square planar geometries, although negative tri- and tetrahydride ions (UH3-, UH4-) adopt structures based on tetrahedral geometries.

Impact Factor: 1.539 Cited Reference Count: 17

Dynamic response of single crystalline copper subjected to quasi-isentropic, gas-gun driven loading

Jarmakani, H., J. M. McNaney, B. Kad, D. Orlikowski, J. H. Nguyen and M. A. Meyers

Materials Science and Engineering a-Structural Materials Properties Microstructure and Processing **463**(1-2): 249-262, 2007.

A transmission electron microscopy study of quasi-isentropic gas-gun loading (peak pressures between 18 and 52GPa) of [0 0 1] monocrystalline copper was carried out. The defect substructures at these different, pressures were analyzed. Current experimental evidence suggests a deformation substructure that transitions from slip to twinning, where twinning occurs at the higher pressures (similar to 52 GPa), and heavily dislocated laths and dislocation cells take place at the intermediate and lower pressures. Evidence of stacking faults at the intermediate pressures was also found. Dislocation cell sizes decreased with increasing pressure and increased with distance away, from the surface of impact. The results from the quasi-isentropic experiments are compared with those for flyer-plate and laser shock experiments reported in the literature. The Preston-Tonks-Wallace constitutive description is used to model both quasi-isentropic and shock compression experiments and predict the pressure at which the slip-twinning transition occurs in both cases. The model predicts a higher twinning transition pressure for isentropic than for shock experiments, and that twinning should not take place in the quasi-isentropic compression experiments given the loading paths investigated. Published by Elsevier B.V.

Impact Factor: 1.490 Cited Reference Count: 26

In situ observations of sigma phase dissolution in 2205 duplex stainless steel using synchrotron X-ray diffraction

Elmer, J. W., T. A. Palmer and E. D. Specht

Materials Science and Engineering a-Structural Materials Properties Microstructure and Processing **459**(1-2): 151-155, 2007.

Synchrotron radiation was used to directly observe the transformation of ferrite, austenite and sigma phases during heating and cooling of 2205 duplex stainless steel. Sigma formed during the initial stages of heating, dissolved as the temperature was increased, and reformed on cooling. The dissolution temperature of sigma was measured to be 985 +/- 2.8 degrees C at a heating rate of 0.25 degrees C/s, and the kinetics of sigma formation at 850 degrees C was determined to be slower after dissolving at 1000 degrees C than before. (C) 2007 Elsevier B.V. All rights reserved.

Impact Factor: 1.490 Cited Reference Count: 17

Spin dependent electron transmission through ferromagnetic thin films

Komesu, T., G. D. Waddill, S. W. Yu and J. G. Tobin

Physics Letters A **368**(1-2): 129-133, 2007.

Spin-polarized electron spectroscopies are used to probe the nature of magnetism in surfaces and thin films. Strong inelastic scattering of the electron from particle-hole and collective excitations results in short mean free paths that can be spin dependent. A quantitative understanding of the spin dependence of the inelastic mean free path is critical to the interpretation of results from spin-polarized electron spectroscopies such as spin-polarized low energy electron diffraction, spin-polarized electron energy loss spectroscopy, and spin-polarized photoemission. Substantial spin asymmetry of the photocurrent has been observed and interpreted as being due to the spin-dependence of the photoelectron inelastic mean free path. We have examined such spin dependent behavior of electrons transmitted though magnetic films with higher kinetic energy in order to reduce complications due to spin-flip scattering, which are more prevalent at lower kinetic energy. We present clear evidence of a spin filter effect for the Ag 3d photoelectrons through a ferromagnetic Fe film at 720 eV (kinetic energy). (c) 2007 Elsevier B.V. All rights reserved.

Impact Factor: 1.468 Cited Reference Count: 22

Effects of grain boundary constraint on properties of polycrystalline materials

McGarrity, E. S., K. S. McGarrity, P. M. Duxbury, B. W. Reed and E. A. Holm

Modelling and Simulation in Materials Science and Engineering **15**(4): S353-S360, 2007.

Grain boundary networks are engineered by increasing the fraction of boundaries which exhibit improved properties. Favourable boundaries have either low grain boundary misorientation or they are special boundaries, such as coincident site lattice boundaries. Significant improvement in properties such as corrosion resistance, critical current in superconductors and mechanical strength and toughness occur, provided percolating grain or grain boundary structures can be engineered. We develop computational models for grain boundary engineered polycrystals and demonstrate that grain boundary constraints modify the behaviour near the percolation threshold. We postulate that this is due to an enhanced clustering of weak boundaries induced by grain boundary constraints. In random grain structures the fraction of strong grain boundaries may be measured in two ways, either the length fraction, c, or the edge fraction c(e). We find that grain boundary constraint shifts the length fraction threshold, c(*), of Potts model polycrystals to higher values, while the edge fraction, c(e*), remains almost the same in both correlated and uncorrelated grain structures.

Impact Factor: 1.457 Cited Reference Count: 25

Enabling strain hardening simulations with dislocation dynamics

Arsenlis, A., W. Cai, M. Tang, M. Rhee, T. Oppelstrup, G. Hommes, T. G. Pierce and V. V. Bulatov

Modelling and Simulation in Materials Science and Engineering **15**(6): 553-595, 2007.

Numerical algorithms for discrete dislocation dynamics simulations are investigated for the purpose of enabling strain hardening simulations of single crystals on massively parallel computers. The algorithms investigated include the O(N) calculation of forces, the equations of motion, time integration, adaptive mesh refinement, the treatment of dislocation core reactions and the dynamic distribution of data and work on parallel computers. A simulation integrating all these algorithmic elements using the Parallel Dislocation Simulator (ParaDiS) code is performed to understand their behaviour in concert and to evaluate the overall numerical performance of dislocation dynamics simulations and their ability to accumulate percent of plastic strain.

Impact Factor: 1.457

A comparison of isoconversional and model-fitting approaches to kinetic parameter estimation and application predictions

Burnham, A. K. and L. N. Dinh

Journal of Thermal Analysis and Calorimetry **89**(2): 479-490, 2007.

A variety of isoconversional and model fitting approaches, all of which use multiple heating schedules, are used to analyze selected data from the ICTAC kinetics and lifetime projects as well as additional simulated data sets created for this work. The objective is to compare the accuracy and suitability of various approaches for various types of chemical reactions. The various simulated data sets show that model fitting and isoconversional methods have comparable reliability for extrapolation outside the range of calibration. First, there is as much variability in prediction for various isoconversional methods as there is between isoconversional methods as a group and different plausible explicit models. Of the three isoconversional models investigated, the Friedman method is usually the most accurate. This is particularly true for energetic materials that have a drop in apparent activation energy in the latter stages of reaction, which leads to a delayed onset of rapid autocatalysis at lower temperatures. It is difficult to determine a priori whether isoconversional or model fitting approaches will give more accurate predictions. The greatest reliability is attained by using both the isoconversional and model fitting approaches on a combination of isothermal and constant heating rate data.

Impact Factor: 1.438

Modeling of Ni-Cr-Mo based alloys: Part II - Kinetics

Turchi, P. E. A., L. Kaufman and Z. K. Liu

CALPHAD-Computer Coupling of Phase Diagrams and Thermochemistry **31**(2): 237-248, 2007.

The CALPHAD approach is applied to kinetic studies of phase transformations and to aging of prototypes of Ni-Cr-Mo-based alloys selected for waste disposal canisters in the Yucca Mountain Project (YMP). Based on a previous study on alloy stability for several candidate alloys, the thermodynamic driving forces, together with a newly developed mobility database, have been used to analyze diffusion-controlled transformations in these Ni-based alloys. Results on precipitation of the Ni2Cr-ordered phase in Ni-Cr and Ni-Cr-Mo alloys, and of the complex P and sigma phases in a surrogate of Alloy 22 are presented, and the output from the modeling are compared with experimental data on aging.

Impact Factor: 1.432 Cited Reference Count: 20

Measurement and prediction of H2O outgassing kinetics from silica-filled polydimethylsiloxane TR55 and S5370

Dinh, L. N., A. K. Burnham, M. A. Schildbach, R. A. Smith, R. S. Maxwell, B. Balazs and W. McLean

Journal of Vacuum Science & Technology A **25**(3): 597-600, 2007.

The isoconversional technique was employed for the measurement and prediction of H2O outgassing kinetics from silica-filled polydimethylsiloxane TR55 and S5370 in a vacuum or dry environment. Isoconversional analysis indicates that the energy barrier for H2O release from TR55 and S5370 is an increasing function of the fractional H2O release. This can be interpreted as the release of H2O from physisorbed water and then chemisorbed water with decreasing OH density from the surfaces of the embedded silica particles. Model-independent predictions of H2O outgassing based on the measured kinetics follow the trend of actual isothermal outgassing at elevated temperatures and suggest gradual outgassing in dry/vacuum storage over many decades at low temperatures for both TR55 and S5370. (C) 2007 American Vacuum Society.

Impact Factor: 1.394 Cited Reference Count: 7

B-doped be coatings for NIF target development

Xu, H., K. A. Moreno, K. P. Youngblood, A. Nikroo, R. E. Hackenberg, J. C. Cooley, C. S. Alford and S. A. Letts

Journal of Vacuum Science & Technology A **25**(4): 1203-1207, 2007.

Sputtered beryllium and copper-doped beryllium coatings as thick as 170 mu m have been deposited on spherical substrates to produce hollow shells that are required as targets for inertial fusion experiments. Be coatings by magnetron sputtering achieved similar to 95 +/- 2% bulk density consistently up to 170 mu m thick. Coatings on the spherical substrates exhibit the typical columnar structure throughout the entire thickness. Transmission electron microscopy indicates the presence of submicron, nearly spherical voids mainly aggregated along the columnar structure and grain boundaries, as well as some smaller intragranular elongated voids. Holes have been drilled in beryllium shells produced in this manner to allow filling with deuterium (the fusion fuel). Gas retention of these shells has been examined using mass spectrometry. It appears that a fraction of the pores in the coatings are interconnected, which leads to leakage of the hollow shells. Boron-doped Be layers near the eutectic phase, at a concentration of similar to 11 at. %, have been added to the Be shells to significantly improve D-2 gas retention of the shells. However, there remains a considerable scatter in the measured leakage. (c) 2007 American Vacuum Society.

Impact Factor: 1.394

Direct observations of sigma phase formation in duplex stainless steels using in-situ synchrotron X-ray diffraction

Elmer, J. W., T. A. Palmer and E. D. Specht

Metallurgical and Materials Transactions A-Physical Metallurgy and Materials Science **38**A(3): 464-475, 2007.

The formation and growth of sigma (sigma) phase in 2205 duplex stainless steel (DSS) was observed and measured in real time using synchrotron radiation during 10 hour isothermal heat treatments at temperatures between 700 degrees C and 850 degrees C. Sigma formed in near-equilibrium quantities during the isothermal holds, starting from a microstructure which contained a balanced mixture of metastable ferrite and austenite. In-situ synchrotron diffraction continuously monitored the transformation, and these results were compared to those predicted by thermodynamic calculations. The data were further analyzed using a modified Johnson-Mehl-Avrami-Kolmogrov (JMAK) approach to determine kinetic parameters for sigma formation over this temperature range. The initial JMAK exponent, n, at low fractions of sigma was found to be approximately 7.0; however, toward the end of the transformation, n decreased to values of approximately 0.75. The change in the JMAK exponent was attributed to a change in the transformation mechanism from discontinuous precipitation with increasing nucleation rate, to growth of the existing sigma phase after nucleation site saturation occurred. Because of this change in mechanism, it was not possible to determine reliable values for the activation energy and pre-exponential terms for the JMAK equation. While cooling back to room temperature, the partial transformation of austenite resulted in a substantial increase in the ferrite content, but sigma retained its high-temperature value to room temperature.

Impact Factor: 1.366 Cited Reference Count: 32

Shock compression of monocrystalline copper: Atomistic Simulations

Cao, B. Y., E. M. Bringa and M. A. Meyers

Metallurgical and Materials Transactions A-Physical Metallurgy and Materials Science **38**A(11): 2681-2688, 2007.

Molecular dynamics (MD) simulations were used to model the effects of shock compression on [001] and [221] monocrystals. We obtained the Hugoniot for both directions, and analyzed the formation of a two-wave structure for the [221] monocrystal. We also analyzed the dislocation structure induced by the shock compression along these two crystal orientations. The topology of this structure compares extremely well with that observed in recent transmission electron microscopy (TEM) studies of shock-induced plasticity in samples recovered from flyer plate and laser shock experiments. However, the density of stacking faults in our simulations is 10(2) to 10(4) times larger than in the experimental observations of recovered samples. The difference between experimentally observed TEM and calculated MD results is attributed to two effects: (1) the annihilation of dislocations during post-shock relaxation (including unloading) and recovery processes and (2) a much shorter stress rise time at the front in MD (< 1 ps) in comparison with flyer-plate shock compression (similar to 1ns).

Impact Factor: 1.366 Cited Reference Count: 31

Orientation relationship, habit plane, twin relationship, interfacial structure, and plastic deformation resulting from the delta -> alpha ‘ isothermal martensitic transformation in Pu-Ga alloys

Moore, K. T., C. R. Krenn, M. A. Wall and A. J. Schwartz

Metallurgical and Materials Transactions A-Physical Metallurgy and Materials Science **38**A(4): 686-697, 2007.

The orientation relationship, habit plane, parent-product interface at the atomic level, twin relationship, and plastic deformation resulting from the delta -> alpha ‘ isothermal martensitic transformation in Pu-Ga alloys are examined using optical microscopy, transmission electron microscopy (TEM), and finite element calculations. The delta -> alpha ‘ transformation exhibits a similar to 20 vol pct collapse when the fcc delta phase transforms to the monoclinic alpha ‘ phase, which results in unique and intriguing crystallography and morphology. Here, we show that the orientation relationship is very close to that previously reported by Zocco et al. (1990), but has small rotational misalignments between the two phases both parallel and perpendicular to the [110](delta)vertical bar vertical bar[100](alpha ‘) direction. The amount of plastic deformation is exceedingly large due to the similar to 20 Vol pct collapse, and TEM is used to quantity the difference in dislocation density between untransformed delta matrix and regions of delta ‘ adjacent to the transformed delta ‘. The twins contained in alpha ‘ plates are shown to have a (205)(alpha) orientation as the lattice invariant deformation and are found to be composed of two alternating variants that share a common < 020 > (alpha ‘) direction, but differ by a 60 deg rotation about < 020 > (alpha ‘). A combination of electron diffraction and optical microscopy has been employed to examine the macroscopic habit plane, and the analysis suggests that a large fraction of the observed habit planes are on or near {111}(delta). Finally, high resolution TEM reveals that the interface is faceted on {111}delta exhibiting a series of terrace and ledaes.

Impact Factor: 1.366 Cited Reference Count: 28

Shock Compression of Monocrystalline Copper: Atomistic Simulations

Cao, B., E. M. Bringa and M. A. Meyers

Metallurgical and Materials Transactions A-Physical Metallurgy and Materials Science, 2007.

Molecular dynamics (MD) simulations were used to model the effects of shock compression on [001] and [221] monocrystals. We obtained the Hugoniot for both directions, and analyzed the formation of a two-wave structure for the [221] monocrystal. We also analyzed the dislocation structure induced by the shock compression along these two crystal orientations. The topology of this structure compares extremely well with that observed in recent transmission electron microscopy (TEM) studies of shock-induced plasticity in samples recovered from flyer plate and laser shock experiments. However, the density of stacking faults in our simulations is 102 to 104 times larger than in the experimental observations of recovered samples. The difference between experimentally observed TEM and calculated MD results is attributed to two effects: (1) the annihilation of dislocations during post-shock relaxation (including unloading) and recovery processes and (2) a much shorter stress rise time at the front in MD (<1 ps) in comparison with flyer-plate shock compression (~1 ns).

Impact Factor: 1.366

Deformation Substructures and Their Transitions in Laser Shock-Compressed Copper-Aluminum Alloys

Meyers, M., M. Schneider, H. Jarmakani, B. Kad, B. Remington, D. Kalantar, J. McNaney, B. Cao and J. Wark

Metallurgical and Materials Transactions A-Physical Metallurgy and Materials Science eFIRST, 2007.

It is shown that the short pulse durations (0.1 to 10 ns) in laser shock compression ensure a rapid decay of the pulse and quenching of the shocked sample in times that are orders of magnitude lower than in conventional explosively driven plate impact experiments. Thus, laser compression, by virtue of a much more rapid cooling, enables the retention of a deformation structure closer to the one existing during shock. The smaller pulse length also decreases the propensity for localization. Copper and copper aluminum (2 and 6 wt pct Al) with orientations [001] and were subjected to high intensity laser pulses with energy levels of 70 to 300 J delivered in an initial pulse duration of approximately 3 ns. The [001] and orientations were chosen, because they respectively maximize and minimize the number of slip systems with highest resolved shear stresses. Systematic differences of the defect substructure were observed as a function of pressure, stacking-fault energy, and crystalline orientation. The changes in the mechanical properties for each condition were compared using micro- and nanohardness measurements and correlated well with observations of the defect substructure. Three regimes of plastic deformation were identified and their transitions modeled: dislocation cells, stacking faults, and twins. An existing constitutive description of the slip to twinning transition, based on the critical shear stress, was expanded to incorporate the effect of stacking-fault energy. A new physically based criterion accounting for stacking-fault energy was developed that describes the transition from perfect loop to partial loop homogeneous nucleation, and consequently from cells to stacking faults. These calculations predict transitions that are in qualitative agreement with the effect of SFE.

Impact Factor: 1.366

Incorporating anisotropic electronic structure in crystallographic determination of complex metals: iron and plutonium

Moore, K. T., D. E. Laughlin, P. Soderlind and A. J. Schwartz

Philosophical Magazine **87**(16-17): 2571-2588, 2007.

Anisotropic electronic structure is incorporated in crystallographic determination of the structure of ferromagnetic Fe, delta-Pu and a Pu-3.7 at% Ga alloy. This is achieved by using anisotropic aspects of the inter-atomic bonds as a motif in combination with the high-symmetry cubic lattice. In the case of Fe, it is shown that ferromagnetic ordering reduces the symmetry of the structure from body centred cubic to body centred tetragonal with an associated effect on elasticity. Thus, the ferromagnetic alpha- and paramagnetic beta- phase are separate and unique phases that should both be addressed on the Fe phase diagrams. In the case of Pu, first-principles density-functional theory calculations are used to show that the bond strengths between the 12 nearest neighbours in delta-plutonium vary greatly. Employing the calculated bond strengths as a motif in crystallographic determination yields a structure with the monoclinic space group Cm for delta-Pu rather than face-centred cubic Fm (3) over barm. The reduced space group for delta-Pu illuminates why it is the only metal with a monoclinic ground state, why lattice distortions of the metal are viable and has implications for the behaviour of the material as it ages due to self-irradiation. Results for a Pu-3.7 at% Ga alloy show that the nearest neighbour bond strengths around a Ga atom are more uniform - a result that explains why Ga stabilizes face-centred cubic delta-Pu. This paper illustrates how an expansion of classical crystallography, which accounts for anisotropic electronic and magnetic structure, can explain complex materials in a novel way.

Impact Factor: 1.354 Cited Reference Count: 54

Dimensional attributes in enhanced hardness of nanocrystalline Ta-V nanolaminates

Jankowski, A. F., J. P. Hayes and C. K. Saw

Philosophical Magazine **87**(16-17): 2323-2334, 2007.

The scaling of microstructure to the nanoscale is a well-known method of enhancing the physical properties of many materials. New findings reveal a 10-fold enhancement in the hardness of nanocrystalline Ta and V nanolaminates is attributable to grain size effects, more so than the layer pair spacing. A Hall-Petch relationship of hardness with grain size appears in these body-centred-cubic nanocrystalline structures.

Impact Factor: 1.354 Cited Reference Count: 23

Fouling study of silicon oxide pores exposed to tap water

Nilsson, J., W. L. Bourcier, J. R. I. Lee and S. E. Letant

Materials Letters **61**(11-12): 2247-2250, 2007.

We report on the fouling of Focused Ion Beam (FIB)-fabricated silicon oxide nanopores after exposure to tap water for two weeks. Pore clogging was monitored by Scanning Electron Microscopy (SEM) on both bare silicon oxide and chemically functionalized nanopores. While fouling occurred on hydrophilic silicon oxide pore walls, the hydrophobic nature of alkane chains prevented clogging on the chemically functionalized pore walls. These results have implications for nanopore sensing platform design.

Impact Factor: 1.353 Cited Reference Count: 12

Interface between quantum-mechanical-based approaches, experiments, and CALPHAD methodology

Turchi, P. E. A., I. A. Abrikosov, B. Burton, S. G. Fries, G. Grimvalle, L. Kaufman, P. Korzhavyi, V. R. Manga, M. Ohno, A. Pisch, A. Scott and W. Q. Zhang

CALPHAD-Computer Coupling of Phase Diagrams and Thermochemistry **31**(1): 4-27, 2007.

The increased application of quantum-mechanical-based methodologies to the study of alloy stability has required a re-assessment of the field. The focus is mainly on inorganic materials in the solid state. In a first part, after a brief overview of the so-called ab initio methods with their approximations, constraints, and limitations, recommendations are made for a good usage of first-principles codes with a set of qualifiers. Examples are given to illustrate the power and the limitations of ab initio codes. However, despite the “success” of these methodologies, thermodynamics of complex multi-component alloys, as used in engineering applications, requires a more versatile approach presently afforded within CALPHAD. Hence, in a second part, the links that presently exist between ab initio methodologies, experiments, and the CALPHAD approach are examined with illustrations. Finally, the issues of dynamical instability and of the role of lattice vibrations that still constitute the subject of ample discussions within the CALPHAD community are revisited in the light of our current knowledge with a set of recommendations.

Impact Factor: 1.344

Shape memory polymers based on uniform aliphatic urethane networks

Wilson, T. S., J. P. Bearinger, J. L. Herberg, J. E. Marion, W. J. Wright, C. L. Evans and D. J. Maitland

Journal of Applied Polymer Science **106**(1): 540-551, 2007.

Aliphatic urethane polymers have been synthesized and characterized, using monomers with high molecular symmetry, to form amorphous networks with very uniform supermolecular structures, which can be used as photo-thermally actuable shape memory polymers (SMPs). The monomers used include hexamethylene diisocyanate (HDI), trimethylhexamethylenediamine (TMHDI), N,N,N',N'-tetrakis(hydroxypropyl)ethylenediamine (HPED), triethanolamine (TEA), and 1,3-butanediol (BD). The new polymers were characterized by solvent extraction, NMR, XPS, UV/VIS, DSC, DMTA, and tensile testing. The resulting polymers were found to be single phase amorphous networks with very high gel fraction, excellent optical clarity, and extremely sharp single glass transitions in the range of 34-153 degrees C. Thermomechanical testing of these materials confirms their excellent shape memory behavior, high recovery force, and low mechanical hysteresis (especially on multiple cycles), effectively behaving as ideal elastomers above T-g We believe these materials represent a new and potentially important class of SMPs, and should be especially useful in applications such as biomedical microdevices. (C) 2007 Wiley Periodicals, Inc.

Impact Factor: 1.306

Compatibility of multi-layer, electrically insulating coatings for vanadium-lithium blankets

Pint, B. A., J. L. Moser, A. Jankowski and J. Hayes

Journal of Nuclear Materials **367**: 1165-1169, 2007.

The objective of this work is to demonstrate that a multi-layer, electrically insulating coating will acceptably reduce the magneto hydrodynamic (MHD) pressure losses in a lithium-cooled blanket. Coatings of Er2O3 or Y2O3 with an overlying coating of vanadium have been fabricated by physical vapor deposition. Coatings have demonstrated acceptable as received resistivity at 800 degrees C in vacuum and at 600 degrees C in contact with Li. When the Y2O3 coating was completely covered with a 10 mu m vanadium layer, it survived exposure to Li for 100 h at 800 degrees C without degradation. The interaction between V alloys and Li at <= 800 degrees C is now the critical compatibility issue and a loop test is being constructed. New ceramic materials based on the Y-Ti-O system also are being explored. Published by Elsevier B.V.

Impact Factor: 1.261 Cited Reference Count: 27

Osmosis in semi-permeable pores: an examination of the basic flow equations based on an experimental and molecular dynamics study

Davis, I. S., B. Shachar-Hill, M. R. Curry, K. S. Kim, T. J. Pedley and A. E. Hill

Proceedings of the Royal Society a-Mathematical Physical and Engineering Sciences **463**(2079): 881-896, 2007.

Classically 'semi-permeable' pores are generally considered to mediate osmotic flow at a rate dependent upon the hydraulic conductance of the pore and the difference in water potential. The shape or size of the solute molecules is not considered to exert a first-order effect on the flow rate nor is the hydraulic conductance thought to be solute dependent. By the experimental measurement of osmosis in the biological pore AQP (aquaporin) and hard-sphere molecular dynamics simulation of a model pore, we show here that the solute radius can have a profound effect on the osmotic flow rate, causing it to decline steeply with decreasing solute radius. Using a simple non-equilibrium thermodynamic theory, we propose that an additional 'osmotic flow coefficient' is required to describe flows in semi-permeable structures such as AQPs, and that the fall in flow rate with radius represents a conversion from hydraulic to diffusive water flow due to increasing penetration of the pore by the solute. The interaction between the pore geometry and the solute size cannot, therefore, be overlooked, although for every solute the system obeys the criterion for semi-permeability required by basic thermodynamics. The osmotic pore theory therefore reveals a novel and potentially rich structure that remains to be explored in full.

Impact Factor: 1.251 Cited Reference Count: 41

Supporting evidence for double-C curve kinetics in the isothermal delta ->alpha phase transformation in a Pu-Ga alloy

Oudot, B., K. Blobaum, M. A. Wall and A. J. Schwartz

Journal of Alloys and Compounds **444**: 230-235, 2007.

Time-temperature-transformation (TTT) diagrams for the delta -> alpha' transformation in a number of Pu-Ga alloys were first reported in 1975 by Orme et al. Unlike typical single-C curve kinetics observed in most isothermal martensitic transformations, the Pu-1.9 at.% Ga alloy exhibits two noses, and thus double-C curve kinetics. The authors attributed the occurrence of the double-C to a difference in mechanism: a massive transformation for the upper C and a martensitic transformation for the lower C. Since that time, the nature, and the existence of the double C have received only limited attention. The results of Deloffre et al. suggest a confirmation of this behavior, but the fundamental origin of the double C remains unknown. Here, we apply differential scanning calorimetry (DSC) as an alternative approach to acquiring the TTT data and our experimental evidence suggests a confirmation of the double-C behavior after 18 h of isothermal hold time. In addition, we report three exothermic peaks corresponding to transformations during cooling at 20 degrees C/min prior to the isothermal holds. These three peaks are reproducible and suggest a number of possibilities for the origin of the unique kinetics: alpha' forms with different morphologies, or from different embryos in the upper and lower C curves; a' forms directly in one C curve and forms via an intermediate phase in the other C curve; the two C curves result from a' forming by two or more distinct mechanisms (e.g., massive and martensitic transformations). F (C) 2006 Elsevier B.V. All rights reserved.

Impact Factor: 1.250 Cited Reference Count: 16

Analysis of density changes in plutonium observed from accelerated aging using Pu-238 enrichment

Chung, B. W., C. K. Saw, S. R. Thompson, T. M. Quick, C. H. Woods, D. J. Hopkins and B. B. Ebbinghaus

Journal of Alloys and Compounds **444**: 329-332, 2007.

We present dimensional and density changes in an aging plutonium alloy enriched with 7.3 at.% of Pu-238 and reference alloys of various ages. After 45 equivalent years of aging, the enriched alloys at 35 degrees C have swelled in length by 0.048-0.052% and now exhibit a near linear dimensional increase, without void swelling. Based on X-ray diffraction measurements, the lattice expansion by self-irradiation appears to be the primary cause for dimensional changes during the initial 2-3 years of aging. Following the initial transient, the density change is primarily cause by a constant helium in-growth rate as a result of a-particle decay. Published by Elsevier B.V.

Impact Factor: 1.250 Cited Reference Count: 6

Atomistic level relativistic quantum modelling of plutonium hydrogen reaction

Balasubramanian, K., T. E. Felter, T. Anklam, T. W. Trelenberg and W. McLean

Journal of Alloys and Compounds **444**: 447-452, 2007.

We have computed the electronic structural and spectroscopic properties for the low-lying electronic states of plutonium hydrides, PuHn (n = 2-4) and their ions which provide significant insight into plutonium hydriding reactions. We have employed a relativistic quantum technique that uses relativistic effective core potentials on Pu. Our computations show that whereas PuH2 and PuH3 form stable C-2v and C-3v structures which exhibit Pu-H direct chemical bonds, PuH4 becomes a complex of PuH2 with a partially dissociated H-2. Our computations show that the H-2 dissociation is assisted by PuH2. Electron density contour maps including Laplacians of charge densities support that the Pu site of the hydrided species is depleted substantially in charge thereby causing catalysis of further hydriding. The IR spectra show that the H-2 sorbed on PuH2 is partially dissociated. We have also provided comparison of our results with corresponding computations on uranium hydrides.

Impact Factor: 1.250 Cited Reference Count: 52

Thermostatics and kinetics of transformations in Pu-based alloys

Turchi, P. E. A., L. Kaufman, S. H. Zhou and Z. K. Liu

Journal of Alloys and Compounds **444**: 28-35, 2007.

CALPHAD assessment of the thermodynamic properties of a series of Pu-based alloys is briefly presented together with some results on the kinetics of phase formation and transformations in Pu-Ga alloys.

Impact Factor: 1.250 Cited Reference Count: 43

Beyond spin-orbit: Probing electron correlation in the Pu 5f states using spin-resolved photoelectron spectroscopy

Tobin, J. G.

Journal of Alloys and Compounds **444**: 154-161, 2007.

Experiments planned to address the issue of electron correlation in the Pu 5f states are described herein. The key is the utilization of the Fano effect: the observation of spin polarization in nonmagnetic systems, using chiral excitation such as circularly polarized X-rays. (c) 2006 Elsevier B.V. All rights reserved.

Impact Factor: 1.250 Cited Reference Count: 29

The search for magnetic order in delta-Pu metal using muon spin relaxation

Heffner, R. H., K. Ohishi, M. J. Fluss, G. D. Morris, D. E. MacLaughlin, L. Shu, B. W. Chung, S. K. McCall, E. D. Bauer, J. L. Sarrao, T. U. Ito and W. Higemoto

Journal of Alloys and Compounds **444**: 80-83, 2007.

We review results from previous muon spin relaxation (mu SR) measurements in applied fields of H-0 = 0 and 0.25 T which established an upper limit for the ordered or disordered frozen spin moment above T = 4 K in delta-Pu (4.3 at.% Ga) of mu(ord) <= 10(-3) mu(B). In addition, we present new data in H-0 = 0.25 and 2 T applied field on a highly annealed delta-Pu (4.3 at.% Ga) sample. Neither the muon Knight shift (H-0 = 2 T) nor the inhomogeneous linewidths in the new sample show appreciable temperature dependence below about T = 60 K, also consistent with no spin freezing. Recent theoretical arguments advanced to explain these results are mentioned. (C) 2006 Elsevier B.V. All rights reserved.

Impact Factor: 1.250 Cited Reference Count: 25

Self-irradiation damage and 5f localization in PuCoGa5

Booth, C. H., M. Daniel, R. E. Wilson, E. D. Bauer, J. N. Mitchell, N. O. Moreno, L. A. Morales, J. L. Sarrao and P. G. Allen

Journal of Alloys and Compounds **444**: 119-123, 2007.

Understanding superconductivity in PuCoGa5 Presents several challenges due to the presence of local moments and self-irradiation damage. We present X-ray absorption fine-structure measurements that further establish the presence of local 5f-electrons. Moreover, these data indicate even stronger localization after the PuCoGa5 sample has aged, indicating a possible mixed valent ground state of the Pu atoms. Local structure measurements on this aged sample show an astonishing amount of damage, approximately 40% of the material after about 2 years. This amount of damage indicates that distortions around the Frenkel defects extend beyond the nearest-neighbor, and is qualitatively consistent with a percolation model for the destruction of the superconducting state after sufficient damage has accumulated. (C) 2006 Elsevier B.V. All rights reserved.

Impact Factor: 1.250 Cited Reference Count: 22

Plutonium and quantum criticality

Chapline, G., M. Fluss and S. McCall

Journal of Alloys and Compounds **444**: 142-144, 2007.

The unusual properties of the elemental plutonium have long been a puzzle. It has been suggested that these properties may be related to quantum criticality [G. Chapline, J.L. Smith, LA Sci. 26 (2000) 1]. In this talk we will describe some experimental observations on rare earth and actinide 14 materials which suggest that there are pairing correlations in all f-electron metals, and that the anomalous properties of the actinides in the vicinity of Np/Pu/Am, even at elevated temperatures, is associated with a critical point in the variation of the pair condensate order parameter with atomic number. (C) 2006 Published by Elsevier B.V.

Impact Factor: 1.250 Cited Reference Count: 22

Isochronal annealing studies in Pu and Pu alloys using magnetic susceptibility

McCall, S. K., M. J. Fluss, B. W. Chung, M. W. McElfresh, G. F. Chapline, D. D. Jackson and R. G. Haire

Journal of Alloys and Compounds **444**: 168-173, 2007.

The isochronal annealing of the low temperature accumulated damage from the radioactive decay of plutonium in alpha-Pu, delta-Pu1-xGax (x = 0.043) and delta-Pu1-xAmx(x = 0.224) was characterized using magnetic susceptibility. In each specimen, thermal annealing, as tracked by magnetic susceptibility, only commenced when T > 33 K and the magnetic susceptibility changes due to defects were fully annealed at T similar to 300 K. The (alpha-Pu magnetic susceptibility isochronal annealing data is similar to earlier measurements of resistivity characterized isochronal annealing. However, the delta-Pu1-xGax = 0.043) magnetic susceptibility isochronal annealing data, when compared with similar resistivity data, indicates that for this alloy magnetic susceptibility studies are more sensitive to vacancies than to the interstitials accumulated at low temperatures. The Pu1-xAmx (x = 0.224) alloy shows a remarkable change in properties, over a limited temperature range beginning where. interstitial defects are first mobile, and characterized by an induced effective moment of order 1.1 mu(B)/Pu. This transient behavior may be evidence for a disorder driven low temperature phase transition, perhaps indicative of a compositional and structural proximity to a state possessing significant magnetic moments.

Impact Factor: 1.250 Cited Reference Count: 19

Proceedings of the Plutonium Futures - The science 2006 conference Pacific Grove, California, USA, 9-13 July 2006

Fluss, M. J., D. E. Hobart, P. G. Allen and G. D. Jarvinen

Journal of Alloys and Compounds **444**: 1-3, 2007.

Impact Factor: 1.250 Cited Reference Count: 0

The optical constants of gallium stabilized delta-plutonium metal between 0.7 and 4.3 eV measured by spectroscopic ellipsometry using a double-windowed experimental chamber

Mookerji, B., M. Stratman, M. Wall and W. J. Siekhaus

Journal of Alloys and Compounds **444**: 339-341, 2007.

A double-windowed vacuum-tight experimental chamber was developed, and calibrated on the spectroscopic ellipsometer over the energy range from 0.7 to 4.5 eV using a silicon wafer with an oxide layer of approximately 25 nm to remove the multiple-window effects from measurements. The plutonium sample (3 mm diameter, 0.1 mm thick) was electro-polished and mounted into the sample chamber in a glove box having a nitrogen atmosphere with less than 100 ppm moisture and oxygen content. The index of refraction n and the extinction coefficient k decrease from 3.7 to 1 and 5.5 to 1.1, respectively as the photon energy increases from 0.7 to 4.3 eV

Impact Factor: 1.250

Density changes in Ga-stabilized delta-Pu, and what they mean

Wolfer, W. G., A. Kubota, P. Soderlind, A. I. Landa, B. Oudot, B. Sadigh, J. B. Sturgeon and M. P. Surh

Journal of Alloys and Compounds **444**: 72-79, 2007.

Ga-stabilized delta-Pu undergoes small changes in density with time. These have been associated with four different causes: an initial reversible expansion that saturates after a short time; a continuous change that can be attributed to the in-growth of helium and actinide daughter products from the radioactive decay of plutonium; possible void swelling; and phase instability. We review our present understanding of these processes and evaluate their contributions to density changes. It is shown that the initial transient expansion is intimately connected with the metastability of the delta-phase at ambient temperature. Published by Elsevier B.V.

Impact Factor: 1.250 Cited Reference Count: 17

Orientation relationship, habit plane, twin relationship, interfacial structure, and plastic deformation resulting from the delta ->alpha ' isothermal martensitic is transformation in Pu-Ga alloys

Moore, K. T., C. R. Krenn, M. A. Wall and A. J. Schwartz

Metallurgical and Materials Transactions a-Physical Metallurgy and Materials Science **38**A(2): 212-222, 2007.

The orientation relationship, habit plane, parent-product interface at the atomic level, twin relationship, and plastic deformation resulting from the delta -> alpha' isothermal martensitic transformation in Pu-Ga alloys are examined using optical microscopy, transmission electron microscopy (TEM), and finite element calculations. The delta -> alpha' transformation exhibits a similar to 20 vol pct collapse when the fcc delta phase transforms to the monoclinic alpha' phase, which results in unique and intriguing crystallography and morphology. Here, we show that the orientation relationship is very close to that previously reported by Zocco et al. (1990), but has small rotational misalignments between the two phases both parallel and perpendicular to the [110](delta) vertical bar vertical bar [100]alpha', direction. The amount of plastic deformation is exceedingly large due to the similar to 20 Vol pct collapse, and TEM is used to quantify the difference in dislocation density between untransformed delta matrix and regions of delta adjacent to the transformed alpha'. The twins contained in alpha' plates are shown to have a (205) (alpha) orientation as the lattice invariant deformation and are found to be composed of two alternating variants that share a common < 020 > (alpha)' direction, but differ by a 60 deg rotation about < 020 > (alpha)'. A combination of electron diffraction and optical microscopy has been employed to examine the macroscopic habit plane, and the analysis suggests that a large fraction of the observed habit planes are on or near {111}(delta). Finally, high resolution TEM reveals that the interface is faceted on {111}(delta) exhibiting a series of terrace and ledges.

Impact Factor: 1.232 Cited Reference Count: 27

Hydrogen diffusion and trapping effects in low and medium carbon steels for subsurface reinforcement in the proposed Yucca Mountain repository

Lamb, J., V. Arjunan, V. Deodeshmukh, D. Chandra, J. Daemen and R. B. Rebak

Metallurgical and Materials Transactions a-Physical Metallurgy and Materials Science **38**A(2): 348-355, 2007.

The electrochemical hydrogen permeation method was used to investigate hydrogen transport, trapping characteristics of low (0.08 pct C) and medium carbon (0.44 pct C) steels proposed for the Yucca Mountain (YM) repository environment. The presence of relatively high amounts of C, Mn, and S increased the density of trapping sites in medium carbon steel. The measured diffusivity of medium carbon steel was lower than that of the low carbon steel due to increased trapping of hydrogen at irreversible sites in the medium carbon steel. Hydrogen concentration values obtained for low carbon steels in YM ground water electrolytes indicate that increased ionic concentration decreases the uptake of hydrogen. The decrease in hydrogen permeation were due the formation of CaCO3 corrosion products on the surface of steels.

Impact Factor: 1.232 Cited Reference Count: 19

Development and applications of multimillijoule soft X-ray lasers

Rus, B., T. Mocek, M. Kozlova, J. Polan, P. Homer, M. Stupka, G. J. Tallents, M. H. Edwards, P. Mistry, D. S. Whittaker, N. Booth, Z. Zhai, G. J. Pert, J. Dunn, A. J. Nelson, M. E. Foord, R. Shepherd, W. Rozmus, H. A. Baldis, M. Fajardo, D. De Lazzari, P. Zeitoun, G. Jamelot, A. Klisnick, D. Ros, K. Cassou, S. Kazamias, H. Bercegol, C. Danson, S. Hawkes, L. Juha, V. Hajkova, J. Chalupsky, J. Feldhaus, H. Wabnitz, J. Nejdl, J. Kuba, M. Davidkova, A. Plavcova and V. Sstisova

Journal of Modern Optics **54**(16-17): 2571-2583, 2007.

We review development of multimillijoule X-ray lasers and of applications of these new laboratory sources carried out recently at the PALS facility. A backbone of this development is the neon-like zinc laser providing saturated output at 21.2 nm, with up to 10 mJ of energy per pulse. This represents currently the most energetic soft X-ray laboratory source. Recent improvements in its operation include better control of the beam shape, and more complete understanding of the prepulse pumping. The laser at 21.2 nm has been employed for a number of application experiments reviewed in this paper. They include transmission measurements of intense soft X-ray radiation, studies of fundamental processes of soft X-ray ablation, ablation micropatterning, feasibility study of soft X-ray Thomson scattering from dense plasmas, visualization of nanometric transient perturbation of optical surfaces, measurements of ablation rates of foils heated by IR pulses, and studies of 2D plasma hydrodynamics in the regime of sequential illumination.

Impact Factor: 1.189 Cited Reference Count: 17

A spin- and angle-resolved photoelectron spectrometer

Mankey, G. J., S. A. Morton, J. G. Tobin, S. W. Yu and G. D. Waddill

Nuclear Instruments & Methods in Physics Research Section A-Accelerators Spectrometers Detectors and Associated Equipment **582**(1): 165-167, 2007.

A spin- and angle-resolved X-ray photoelectron spectrometer for the study of magnetic materials will be discussed. It consists of a turntable with electron lenses connected to a large hemispherical analyzer. A Mini-Mott spin detector is fitted to the output of the hemispherical analyzer. This system, when coupled to a synchrotron radiation source will allow determination of a complete set of quantum numbers of a photoelectron. This instrument will be used to study ferromagnetic, antiferromagnetic and nonmagnetic materials.

Impact Factor: 1.185 Cited Reference Count: 13

Spin Spectrometer at the ALS and APS

Tobin, J. G., S. A. Morton, S. W. Yu, T. Komesu, G. D. Waddill and P. Boyd

Nuclear Instruments & Methods in Physics Research Section A-Accelerators Spectrometers Detectors and Associated Equipment **582**(1): 162-164, 2007.

A spin-resolving photoelectron spectrometer, the "Spin Spectrometer," has been designed and built. It has been utilized at both the Advanced Light Source in Berkeley, CA, and the Advanced Photon Source in Argonne, IL. Technical details and an example of experimental results are presented here. (C) 2007 Elsevier B.V. All rights reserved.

Impact Factor: 1.185 Cited Reference Count: 11

Molecular dynamics simulation of amorphization in forsterite by cosmic rays

Devanathan, R., P. Durham, J. Du, L. R. Corrales and E. M. Bringa

Nuclear Instruments & Methods in Physics Research Section B-Beam Interactions with Materials and Atoms **255**(1): 172-176, 2007.

We have examined cosmic ray interactions with silicate dust grains by simulating a thermal spike in a 1.25 million atom forsterite (Mg2SiO4) crystal with periodic boundaries. Spikes were generated by giving a kinetic energy of I or 2 eV to every atom within a cylinder of radius 1.73 mn along the [001] direction. An amorphous track of radius similar to 3 nm was produced for the 2 eV/atom case, but practically no amorphization was produced for I eV/atom because of effective dynamic annealing. Chemical segregation was not observed in the track. These results agree with recent experimental studies of ion irradiation effects in silicates, and indicate that cosmic rays can cause the amorphization of interstellar dust. (c) 2006 Published by Elsevier B.V.

Impact Factor: 1.181 Cited Reference Count: 14

Atomistic simulations of swift ion tracks in diamond and graphite

Schwen, D. and E. M. Bringa

Nuclear Instruments & Methods in Physics Research Section B-Beam Interactions with Materials and Atoms **256**(1): 187-192, 2007.

We have used molecular dynamics simulations to study ion tracks in diamond and graphite. Tracks are included using a thermal spike model, i.e. a certain number of atoms within an initial track radius are given an initial excitation energy. The total energy given to the excited atoms and the length of the track determine an "effective" stopping power dE/dx. Electronic excitations in semiconductors and semimetals like diamond and graphite can diffuse far from each other or be quenched before they couple to the lattice. This effect is included by varying the number of atoms that are effectively energized within the track. We use an initial track radius of 3 nm and we find that full amorphization of this region during the first few ps only occurs when the "effective" dE/dx is larger than 6 +/- 0.9 keV/nm for graphite and 10.5 +/- 1.5 keV/nm for diamond. Since the "effective" dE/dx depends on the electron-phonon coupling, our simulations set bounds on the efficiency of the coupling between the electronic excitations and the lattice in this highly non-equilibrium scenario.

Impact Factor: 1.181

Damage buildup and the molecular effect in Si bombarded with PFn cluster ions

Titov, A. I., A. Y. Azarov, L. M. Nikulina and S. O. Kucheyev

Nuclear Instruments & Methods in Physics Research Section B-Beam Interactions with Materials and Atoms **256**(1): 207-210, 2007.

We study the molecular effect (ME) in damage accumulation in Si bombarded at room temperature with atomic P and F and cluster PFn (n = 2 and 4) ions with an energy of 2.1 keV/amu. Correct ion irradiation conditions for unambiguous studies of the ME are discussed. Rutherford backscattering/channeling spectrometry results show that the damage buildup behavior strongly depends on the cluster ion size, and the ME efficiency increases rapidly with increasing the number of atoms in cluster ions. Moreover, the ME efficiency decreases with increasing the defect generation rate, indicating that dynamic annealing processes, rather than nonlinear energy spikes, play a major role in the ME for these irradiation conditions.

Impact Factor: 1.181

Fluctuations and Gibbs-Thomson law - the simple physics

Chernov, A. A., J. J. De Yoreo and L. N. Rashkovich

Journal of Optoelectronics and Advanced Materials **9**(5): 1191-1197, 2007.

Crystals of slightly soluble materials should be subject of relatively weak attachment/detachment fluctuations on their faces so that steps on those faces have low kink density. These steps are parallel to the most close packed lattice rows and form polygons on a crystal surface. The process responsible for implementation of the classical Gibbs-Thomson law (GTL) for the polygonal step (in two dimensions, 2D) is kink exchange between the step corners. For the 3D crystallites, this mechanism includes step exchange. If these mechanisms do not operate because of slow fluctuations, the GTL is not applicable. Physics of these processes and conditions for the GTL applicability are discussed on a simple qualitative level.

Impact Factor: 1.106 Cited Reference Count: 20

Morphology, microstructure, and residual stress in EBPVD erbia coatings

Jankowski, A. F., C. K. Saw, J. L. Ferreira, J. S. Harper, J. P. Hayes and B. A. Pint

Journal of Materials Science **42**(14): 5722-5727, 2007.

The electron-beam physical vapor deposition of erbium-oxide coatings onto sapphire wafers is investigated to evaluate processing effects on the residual stress state and microstructure. The erbium-oxide coatings are found to be in a compressive stress state. The crystallographic texture of the erbium-oxide coating is evaluated using X-ray diffraction along with an assessment of forming the cubic erbia phase as a function of substrate temperature. In addition to the cubic erbia phase, an orthorhombic phase is found at the lower deposition temperatures. A transition is found from a two-phase erbium-oxide coating to a single phase at deposition temperatures above 948 K. The variation in morphology with deposition temperature observed in fracture cross-sections is consistent with features of the classic zone growth models for vapor-deposited oxide coatings. For high-temperature applications, a deposition process temperature above 948 K is seen to produce a stoichiometric, fully dense, and equiaxed-polycrystalline coating of cubic erbia.

Impact Factor: 0.999 Cited Reference Count: 32

Abnormal strain hardening in nanostructured titanium at high strain rates and large strains

Wang, Y. M., J. Y. Huang, T. Jiao, Y. T. Zhu and A. V. Hamza

Journal of Materials Science **42**(5): 1751-1756, 2007.

Commercial purity nanostructured titanium prepared by equal channel angular pressing plus cold rolling (grain size similar to 260 nm) exhibits a nonnegligible strain hardening behavior at large compressive strains (> 15%) and quasistatic loading conditions. The degree of the strain hardening increases with increasing strain rates and becomes more pronounced at dynamic loading rates. This behavior is in contrast with what we have seen so far in other nanostructured materials, where flat stress-strain curves are often seen. It was concluded from transmission electron microscopy investigations that in addition to dislocation slips, deformation twinning may have played a significant role in plastic deformation of nanostructured Ti. The structural failure behavior is in-situ recorded by a CCD camera and reasoned according to the microscopic observations.

Impact Factor: 0.901 Cited Reference Count: 17

Anodic behavior of specimens prepared from a full-diameter alloy 22 fabricated mockup container for nuclear waste

Estill, J. C. and R. B. Rebak

Journal of Pressure Vessel Technology-Transactions of the ASME **129**(4): 729-736, 2007.

Alloy 22 (N06022) has been extensively tested for general and localized corrosion behavior both in the wrought annealed condition and in the as-welded condition. In general, the specimens for laboratory testing are mostly prepared from flat plates of material. It is important to determine if the process of fabricating a container will affect the corrosion performance of this alloy. Thus, specimens for corrosion testing were prepared directly from a fabricated full-diameter Alloy 22 container Results show that both the anodic corrosion behavior and the localized corrosion resistance of specimens prepared from a welded container were the same as those from flat welded plates.

Impact Factor: 0.843 Cited Reference Count: 14

A comprehensive theory of yielding and failure for isotropic materials

Christensen, R. M.

Journal of Engineering Materials and Technology-Transactions of the Asme **129**(2): 173-181, 2007.

A theory of yielding and failure for homogeneous and isotropic materials is given. The theory is calibrated by two independent, measurable properties and from those it predicts possible failure for any given state of stress. It also differentiates between ductile yielding and brittle failure. The explicit ductile-brittle criterion depends not only upon the material specification through the two properties, but also and equally importantly depends upon the type of imposed stress state. The Mises criterion is a special (limiting) case of the present theory. A close examination of this case shows that the Mises material idealization does not necessarily imply ductile behavior under all conditions, only under most conditions. When the first invariant of the yield/failure stress state is sufficiently large relative to the distortional part, brittle failure will be expected to occur For general material types, it is shown that it is possible to have a state of spreading plastic flow, but as the elastic-plastic boundary advances, the conditions for yielding on it can change over to conditions for brittle failure because of the evolving stress state. The general theory is of a three-dimensional, form and it applies to full density materials for which the yield/failure strength in uniaxial tension is less than or at most equal to the magnitude of that in uniaxial compression.

Impact Factor: 0.816

The computational modeling of alloys at the atomic scale: from ab initio and thermodynamics to radiation-induced heterogeneous precipitation

Caro, A., M. Caro, P. Klaver, B. Sadigh, E. M. Lopasso and S. G. Srinivasan

JOM **59**(4): 52-57, 2007.

This paper describes a strategy to simulate radiation damage in FeCr alloys wherein magnetism introduces an anomaly in the heat of formation of the solid solution. This has implications for the precipitation of excess chromium in the alpha' phase in the presence of heterogeneities. These complexities pose many challenges for atomistic (empirical) methods. To address such issues the authors have developed a modified many body potential by rigorously fitting thermodynamic properties including free energy. Multi-million atom displacement Monte Carlo simulations in the transmutation ensemble, using the new potential, predict that thermodynamically grain boundaries, dislocations, and free surfaces are not preferential sites for alpha' precipitation.

Impact Factor: 0.692 Cited Reference Count: 27

Effect of fluoride ions on crevice corrosion and passive behavior of alloy 22 in hot chloride solutions

Carranza, R. M., M. A. Rodriguez and R. B. Rebak

Corrosion **63**(5): 480-490, 2007.

Alloy 22 (UNS N06022) is a Ni-Cr-Mo-W alloy highly resistant to localized corrosion. Alloy 22 may be susceptible to crevice corrosion in pure chloride (Cl-) solutions under aggressive environmental conditions. The effect of the fluoride (F-) over the crevice corrosion induced by chloride ions is still not well established. The objective of the present work was to explore the crevice corrosion resistance of this alloy to different mixtures of fluorides and chlorides. Cyclic potentiodynamic polarization (CPP) tests were conducted in deaerated aqueous solutions of pure halide ions and in different mixtures of chloride and fluoride at 90 degrees C and pH 6. The range of chloride concentration [Cl-] was 0.001 M <= [Cl-] <= 10 M and the range of fluoride to chloride molar concentration ratio [F-]1[Cl-] was 0. 1 :5 [F-]/[Cl-] <= 10. Results show that Alloy 22 was susceptible to crevice corrosion in all the pure chloride solutions but was not in the pure fluoride solutions. Fluoride ions showed an inhibitor behavior only in mixtures with a molar ratio [F-]/[Cl-] > 2. For mixtures with a molar ratio [F-]/[Cl-] of 7 and 10, the inhibition of crevice corrosion was complete.

Impact Factor: 0.687 Cited Reference Count: 33

Removal of the mandrel from beryllium sputter coated capsules for NIF targets

Bhandarkar, S., S. A. Letts, S. Buckley, C. Alford, E. Lindsey, J. Hughes, K. P. Youngblood, K. Moreno, H. Xu, H. Huang and A. Nikroo

Fusion Science and Technology **51**(4): 564-571, 2007.

The choice of the mandrel material has a significant bearing on the properties of the sputter-coated beryllium shell needed for NIF targets. Here, we present our work on screening four mandrel materials, their impact on the Be shell and issues related to their subsequent removal. Beryllium shells sputter deposited on hollow glow discharge polymer or GDP spheres met most of the target specifications. However, they had greater opacity due to partial oxidation of the Be during the GDP burnout step. Poly (a-methyl styrene), silicon and nickel beads were explored as alternative mandrels but were plagued with problems such as cracking of the Be shell or incomplete removal. The most promising approach was a two-step coating process mediated by a thin 6,um Be mandrel that is made using GDP.

Impact Factor: 0.678

Fabrication of double shell targets with a glass inner capsule supported by SiO2 aerogel for shots on the Omega laser in 2006

Bono, M., D. Bennett, C. Castro, J. Satcher, J. Poco, B. Brown, H. Martz, N. Teslich, R. Hibbard, A. Hamza, P. Amendt, H. Robey, J. Milovich and R. Wallace

Fusion Science and Technology **51**(4): 611-625, 2007.

Indirectly driven double shell implosions are being investigated as a possible noncryogenic path to ignition on the National Ignition Facility. Lawrence Livermore National Laboratory has made several technological advances that have produced double shell targets that represent a significant improvement to previously fielded targets. The inner capsule is supported inside the ablator shell by SiO2 aerogel with a nominal density of 50 mg/cm(3). The aerogel is cast around the inner capsule and then machined concentric to it. The seamless sphere of aerogel containing the embedded capsule is then assembled between the two halves of the ablator shell. The concentricity between the two shells has been improved to less than 1.5 mu m. The ablator shell consists of two hemispherical shells that mate at a step joint that incorporates a gap with a nominal thickness of 0.1 mu m. Using a new flexure-based tool holder that precisely positions the diamond cutting tool on the diamond turning machine, step discontinuities on the inner surface of the ablator of less than 0.5 mu m have been achieved. New methods have been used to comprehensively characterize each of the targets using high-resolution x-ray imaging systems.

Impact Factor: 0.678

Investigation of deuterium permeability of sputtered beryllium and graded copper-doped beryllium shells

Nikroo, A., H. W. Xu, K. A. Moreno, K. P. Youngblood, J. Cooley, C. S. Alford, S. A. Letts and R. C. Cook

Fusion Science and Technology **51**(4): 553-558, 2007.

Graded copper-doped Be shells have been fabricated by sputter coating on spherical mandrels. While such coatings have consistent microstructure and acceptable void content and size, we have found that they suffer from sufficient interconnected porosity leading to relatively rapid gas leakage. In this paper, we present an extensive study of D-2 leakage out of Be shells made by sputter coating. The leakage appears to follow molecular flow dynamics as determined by examining the temperature dependence of the flow. Furthermore, the time dependence of the leakage suggests that the flow channels are nanometerish in diameter, propagating through the thickness of the coating, possibly brought about by residual stress in the coatings. We have investigated the D2 leakage time constant as a function of a large number of coating parameters, including the effect of introducing boron-doped layers. Addition of thin 0.25 mu m amorphous boron-doped layers near the inside surface has been most effective in producing shells with long time constants (greater than 7 days to immeasurable) with yield of greater than 50%. There is still substantial scatter in the data, even within a given coating batch, suggesting a possible stochastic cracking process driven by residual stress in the coating.

Impact Factor: 0.678

Beryllium capsule coating development for NIF targets

Xu, H. W., C. S. Alford, J. C. Cooley, L. A. Dixon, R. E. Hackenberg, S. A. Letts, K. A. Moreno, A. Nikroo, J. R. Wall and K. P. Youngblood

Fusion Science and Technology **51**(4): 547-552, 2007.

Various morphologies have been observed in sputter-deposited Be ablator capsules, including nodular growth, cone growth and twisted grain growth. By devising an agitation method that includes both bouncing and rolling the spherical mandrels during deposition, and by reducing the coating rate, consistent columnar grain structure has now been obtained up to 170 mm. Low mode deformation of the shells is observed on thin CH mandrels, but is suppressed if stiffer mandrels are used. Ablator density measured by weighing and x-ray radiography is 93%-95% of bulk density of Be. Transmission electron microscopy shows 100-200nm size voids in the film and striations inside the grains. Be shells produced with rolling agitation have met most Of the NIF specifications. Some of the few remaining issues will be discussed.

Impact Factor: 0.678

Removal of GDP mandrels from sputter-coated beryllium capsules for NIF targets

Youngblood, K. P., K. A. Moreno, A. Nikroo, H. Huang, Y. T. Lee, S. A. Letts, C. S. Alford and S. R. Buckley

Fusion Science and Technology **51**(4): 572-575, 2007.

Ablative targets for the National Ignition Campaign (NIC) have been fabricated by sputter coating spherical mandrels made of glow discharge polymer (GDP) with graded copper doped beryllium (Be) layers. The inner mandrel must be completely removed to meet specific ignition design requirements. The process of removing the mandrel requires elevated temperature in the presence of oxygen. However, elevating the temperature in air also oxidizes the Be and can cause blistering on the inner surface of the Be shell. This paper will discuss a refined technique, which removes the GDP mandrel without compromising the integrity of the inner Be surface. The oxygen gradient that develops during the mandrel removal and the impact of its presence will also be discussed.

Impact Factor: 0.678

Kinetic Monte Carlo modelling of neutron irradiation damage in iron

Gamez, L., E. Martinez, J. M. Perlado, P. Cepas, M. J. Caturla, M. Victoria, J. Marian, C. Arevalo, M. Hernandez and D. Gomez

Fusion Engineering and Design **82**(15-24): 2666-2670, 2007.

Ferritic steels (FeCr based alloys) are key materials needed to fulfill the requirements expected in future nuclear fusion facilities, both for magnetic and inertial confinement, and advanced fission reactors (GIV) and transmutation systems. Research in such field is actually a critical aspect in the European research program and abroad. Experimental and multiscale simulation methodologies are going hand by hand in increasing the knowledge of materials performance. At DENIM, it is progressing in some specific part of the well-linked simulation methodology both for defects energetics and diffusion, and for dislocation dynamics. In this study, results obtained from kinetic Monte Carlo simulations of neutron irradiated Fe under different conditions are presented, using modified ad hoc parameters. A significant agreement with experimental measurements has been found for some of the parameterization and mechanisms considered. The results of these simulations are discussed and compared with previous calculations.

Impact Factor: 0.598 Cited Reference Count: 14

Accurate mean field void bias factors for radiation swelling calculations

Surh, M. P. and W. G. Wolfer

Journal of Computer-Aided Materials Design **14**(3): 419-424, 2007.

A fast numerical approximation is introduced for the interaction of vacancies and interstitials with a spherical cavity in an isotropic elastic medium. The image interaction is evaluated from a fit which is accurate and simple enough to obtain bias factors for rate theories of radiation swelling by direct numerical integration.

Impact Factor: 0.591 Cited Reference Count: 6

Characterisation of electron beams at different focus settings and work distances in multiple welders using the enhanced modified Faraday cup

Palmer, T. A. and J. W. Elmer

Science and Technology of Welding and Joining **12**(2): 161-174, 2007.

Using the enhanced modified Faraday cup (EMFC), the differences in the beams produced by two electron beam welders are characterised at different focus settings and work distances. For example, EMFC measurements show that sharply focused beams display different shapes and peak power densities which vary by nearly 20% for the same welding parameters on these two welders. Increases in work distance on each machine were shown to result in decreases in both the peak power density and the resulting weld size and shape. Because of the differences in machine performance, additional differences also arise when comparing the welds produced by each machine. These different weld dimensions are attributed to differences in the beam shape and a 70 mm difference in the theoretical beam crossover location in the upper column of the two welders. The crossover location, which can not be physically measured, is determined using the EMFC by analysing the beam distribution parameters of sharply focused beams over a range of work distances. By combining these results with simplified optics calculations, the magnification of the beam optics can be determined and the machine performance of each welder characterised. The work distance on each machine at which beams with similar peak power density values will be produced can then be determined. With this knowledge, changes in either the beam focus or work distance can be made to attain similar beams from different welders, thus providing a baseline for developing modern weld transfer procedures.

Impact Factor: 0.590 Cited Reference Count: 22

Modeling planetary interiors in laser based experiments using shockless compression

Hawreliak, J., J. Colvin, J. Eggert, D. H. Kalantar, H. E. Lorenzana, S. Pollaine, K. Rosolankova, B. A. Remington, J. Stolken and J. S. Wark

Astrophysics and Space Science **307**(1-3): 285-289, 2007.

X-ray diffraction is a widely used technique for measuring the crystal structure of a compressed material. Recently, short pulse x-ray sources have been used to measure the crystal structure in-situ while a sample is being dynamically loaded. To reach the ultra high pressures that are unattainable in static experiments at temperatures lower than using shock techniques, shockless quasi-isentropic compression is required. Shockless compression has been demonstrated as a successful means of accessing high pressures. The National Ignition Facility (NIF), which will begin doing high pressure material science in 2010, it should be possible to reach over 2 TPa quasi-isentropically. This paper outlines how x-ray diffraction could be used to study the crystal structure in laser driven, shocklessly compressed targets the same way it has been used in shock compressed samples. A simulation of a shockless laser driven iron is used to generate simulated diffraction signals, and recent experimental results are presented.

Impact Factor: 0.495 Cited Reference Count: 21

Untitled

Chang, Y. A., R. Schmid-Fetzer and P. E. A. Turchi

Journal of Phase Equilibria and Diffusion **28**(1): 1-1, 2007.

Impact Factor: 0.427 Cited Reference Count: 0

Transferring electron beam welding parameters using the enhanced modified faraday cup

Palmer, T. A., J. W. Elmer, K. D. Nicklas and T. Mustaleski

Welding Journal **86**(12): 388S-398S, 2007.

Impact Factor: 0.350 Cited Reference Count: 15

Reduction of HAuCl4 by Na2S revisited: The case for Au nanoparticle aggregates and against Au2S/Au Core/Shell particles

Schwartzberg, A. M., C. D. Grant, T. van Buuren and J. Z. Zhang

Journal of Physical Chemistry C **111**(25): 8892-8901, 2007.

The reaction of sodium sulfide with chloroauric acid has been surrounded by a controversy over the structure of the resulting product. The original report proposed a Au2S/Au core/shell structure based on strong near-IR resonance and limited transmission electron microscopy. Subsequent reports used the same model without further attempts to determine the structure of the products. With a significant body of experimental work compiled over a period of several years, we have shown that the major product of this reaction is aggregated spherical nanoparticles of gold with a minority component consisting of triangular and rod-like structures. This is in contradiction to the core/shell structures as originally proposed. Recently, there have been additional reports that again suggest a Au2S/Au core/shell structure or irregularly shaped Au nanoparticles as an explanation for the near-IR resonance. To help resolve this issue, we have carried out further experiments to determine how the reaction products may depend on experimental conditions such as concentration and aging of the reactants, particularly Na2S. It has been determined that sodium thiosulfate is the likely product from Na2S aging. In addition, persistent spectral hole burning experiments have been conducted on gold nanoparticle aggregate (GNA) samples at excitation intensities that are lower than that required to melt the nanostructures. We have observed a decrease in optical absorption on resonance with the excitation laser wavelength, with simultaneous increases in absorption to the blue and red of this wavelength region. However, in the presence of the stabilizer poly(vinyl pyrrolidone) (PVP), no increase in absorbance was observed but rather a blue shifting and decrease in intensity of the near-IR plasmon resonance. These results imply that the non-stabilized GNAs are able to break apart and reform into off resonant aggregate structures. In contrast, this behavior is suppressed in PVP stabilized GNAs because of the presence of polymer which quickly passivates the individual nanoparticles that comprise the GNAs after they are disrupted by laser irradiation. These results would be very difficult to explain if the nanostructures were core/shell. Therefore, these new results again support the model of GNAs as the best possible explanation for the product of the HAuCl4 and Na2S reaction.

Impact Factor: NEW IN 2007 Cited Reference Count: 105

Universal phenomena of CO adsorption on gold surfaces with low-coordinated sites

Yim, W. L., T. Nowitzki, M. Necke, H. Schnars, P. Nickut, J. Biener, M. M. Biener, V. Zielasek, K. Al-Shamery, T. Kluner and M. Baumer

Journal of Physical Chemistry C **111**(1): 445-451, 2007.

Since Au turned out to be an active catalyst for CO oxidation at low temperatures, CO adsorption on various Au surfaces has been in the scope of numerous surface science studies. Interestingly, supported particles as well as stepped and rough single-crystal surfaces exhibit very similar adsorption behavior. To elucidate the origin of these similarities, we have performed temperature-programmed desorption and infrared absorption spectroscopy for a whole range of Au surfaces from nanoparticles grown on HOPG to Au(111) surfaces roughened by argon ion bombardment. In line with previous results, we have observed two desorption states at similar to 130-145 and similar to 170-185 K, respectively, and one infrared peak at around 2120 cm(-1) in all cases. In addition to the experiments, we have carried out theoretical studies of CO adsorption on Au(332). The calculations show that CO desorption states above 100 K may be located at step-edges but not on terrace sites. Reducing the coordination of Au atoms further leads to successively higher binding energies with an unchanged anharmonic frequency. Therefore, we conclude that both desorption peaks belong to CO on low-coordinated Au atoms at steps and kinks. For the sputtered Au(111) surface, scanning tunneling microscopy reveals a rough pit-and-mound morphology with a large number of such sites. In annealing experiments we observe that the loss of these sites coincides with the loss of CO adsorption capacity, corroborating our conclusions.

Impact Factor: NEW IN 2007 Cited Reference Count: 38

Breakdown of self-similar hardening Behavior in Au nanopillar microplasticity

Marian, J. and J. Knap

International Journal for Multiscale Computational Engineering **5**(3-4): 287-294, 2007.

This article is concerned with the study of scale effects in Au nanopillars under compression. We propose that plastic yielding in these nanostructures is characterized by a critical length scale at which a transition from volumetric to surface-dominated plasticity takes place. This transition effectively sets a lower bound on the self-similar behavior commonly assumed in nanostrength models. Using quasi-continuum simulations, we study the subcritical regime and find that plasticity at these scales is governed by dislocation emission at surface irregularities.

Impact Factor: N/A Cited Reference Count: 45

Multilayers for next generation x-ray sources

Bajt, S., H. N. Chapman, E. Spiller, S. Hau-Riege, J. Alameda, A. J. Nelson, C. C. Walton, B. Kjornrattanawanich, A. Aquila, F. Dollar, E. Gullikson, C. Tarrio and S. Grantham

Damage to VUV, EUV, and X-Ray Optics, L. Juha, R. H. Sobierajski and H. Wabnitz, ed., **6586**: U135-U144 (2007).

Multilayers are artificially layered structures that can be used to create optics and optical elements for a broad range of x-ray wavelengths, or can be optimized for other applications. The development of next generation x-ray sources (high brightness synchrotrons and x-ray free electron lasers) requires advances in x-ray optics. Newly developed multilayer-based mirrors and optical elements enabled efficient band-pass filtering, focusing and time resolved measurements in recent FLASH (Free Electron LASer in Hamburg) experiments. These experiments are providing invaluable feedback on the response of the multilayer structures to high intensity, short pulsed x-ray sources. This information is crucial to design optics for future x-ray free electron lasers and to benchmark computer codes that simulate damage processes.

Impact Factor: N/A Cited Reference Count: 43

Terahertz radiation from shocked materials

Reed, E. J., M. R. Armstrong, K. Kim, M. Soljacic, R. Gee, J. H. Glownia and J. D. Joannopoulos

Materials Today **10**(7-8): 44-50, 2007.

Distinct physical mechanisms for the generation of temporally coherent, narrow bandwidth optical radiation are few and rare in nature. Such sources, including lasers, have widespread applications ranging from spectroscopy to interferometry. We review the recent theoretical prediction of a new type of temporally coherent optical radiation source in the 1-100 THz frequency range that can be realized when crystalline polarizable materials like NaCl are subject to a compressive shock wave.

Impact Factor: N/A Cited Reference Count: 31

Synthesis and characterization of nitrides of iridium and palladium

Crowhurst, J., A. Goncharov, B. Sadigh, J. Zaug, Y. Meng and V. Prakapenka

Materials Research at High Pressure. M. R. Manaa, A. F. Goncharov, R. J. Hemley and R. Bini. **987**: 3-9, 2007.

Impact Factor: N/A

Physical property changes in plutonium observed from accelerated aging using Pu-238 enrichment

Chung, B. W., B. Choi, C. Saw, S. Thompson, C. Woods, D. Hopkins and B. Ebbinghaus

Actinides 2006-Basic Science, Applications and Technology. K. J. M. Blobaum, E. A. Chandler, L. Havela, M. B. Maple and M. P. Neu. **986**: 143-147, 2007.

Impact Factor: N/A

Radiation damage effects on the magnetic properties of Pu(1-x)Amx (x=0.224)

McCall, S. K., M. J. Fluss, B. W. Chung, M. W. McElfresh and R. G. Haire

Actinides 2006-Basic Science, Applications and Technology. K. J. M. Blobaum, E. A. Chandler, L. Havela, M. B. Maple and M. P. Neu. **986**: 107-111, 2007.

Impact Factor: N/A

Comparative experimental study of X-ray absorption spectroscopy and electron energy loss spectroscopy on passivated U surfaces

Nelson, A. J., W. J. Moberlychan, R. A. Bliss, W. J. Siekbaus, T. E. Feller and J. D. Denlinger

Actinides 2006-Basic Science, Applications and Technology. K. J. M. Blobaum, E. A. Chandler, L. Havela, M. B. Maple and M. P. Neu. **986**: 101-105, 2007.

Impact Factor: N/A

Changes in delta-plutonium due to aging as observed by continuous in-situ X-ray scattering

Saw, C. K., M. A. Wall and B. W. Chung

Actinides 2006-Basic Science, Applications and Technology. K. J. M. Blobaum, E. A. Chandler, L. Havela, M. B. Maple and M. P. Neu. **986**: 137-141, 2007.

Impact Factor: N/A

On the electronic configuration in Pu

Tobin, J. G., P. Soderlind, A. Landal, K. T. Moore, A. J. Schwartz, B. W. Chung, M. A. Wait, J. M. Wills, R. G. Haire and A. L. Kutepov

Actinides 2006-Basic Science, Applications and Technology. K. J. M. Blobaum, E. A. Chandler, L. Havela, M. B. Maple and M. P. Neu. **986**: 29-34, 2007.

Impact Factor: N/A

Effects of long-term service on the aging behavior of a water-quenched U6Nb alloy

Zhou, J. K. and L. L. Hsiung

Actinides 2006-Basic Science, Applications and Technology. K. J. M. Blobaum, E. A. Chandler, L. Havela, M. B. Maple and M. P. Neu. **986**: 157-165, 2007.

Impact Factor: N/A

Repassivation potential of alloy 22 in chloride plus nitrate solutions using the potentiodynamic-galvanostatic-potentiostatic method

Evans, K. J. and R. B. Rebak

30th Symposium on Scientific Basis for Nuclear Waste Management, D. Dunn, C. Poinssot and B. Begg, ed., **985**: 313-320 (2007).

In general, the susceptibility of Alloy 22 to suffer crevice corrosion is measured using the Cyclic Potentiodynamic Polarization (CPP) technique. This is a fast technique that gives rather accurate and reproducible values of repassivation potential (ER1) in most cases. In the fringes of susceptibility, when the environment is not highly aggressive, the values of repassivation potential using the CPP technique may not be highly reproducible, especially because the technique is fast. To circumvent this, the repassivation potential of Alloy 22 was measured using a slower method that combines Potentiodynamic-Galvanostatic-Potentiostatic steps (called here the Tsujikawa-Hisamatsu Electrochemical or THE method). The THE method applies the charge to the specimen in a more controlled way, which may give more reproducible repassivation potential values, especially when the environment is not aggressive. The values of repassivation potential of Alloy 22 in sodium chloride plus potassium nitrate solutions were measured using the THE and CPP methods. Results show that both methods yield similar values of repassivation potential, especially under aggressive conditions.

Cited Reference Count: 30

Mechanisms of inhibition of crevice corrosion in alloy 22

Rebak, R. B.

30th Symposium on Scientific Basis for Nuclear Waste Management, D. Dunn, C. Poinssot and B. Begg, ed., **985**: 261-268 (2007).

Alloy 22 may be susceptible to crevice corrosion in chloride-containing environments, especially at temperatures above ambient. The presence of oxyanions, especially nitrate, minimizes or eliminates the susceptibility of Alloy 22 to crevice corrosion. Other anions such as sulfate, carbonate and fluoride were also reported as inhibitors of crevice corrosion in Alloy 22. It is argued that the occurrence of crevice corrosion is due to the formation of hydrochloric acid solution in the creviced region. Inhibitors act by eliminating the occurrence of hydrochloric acid or by hampering its action.

Cited Reference Count: 28

A high-performance corrosion-resistant iron-based amorphous metal-the effects of composition, structure and environment on corrosion resistance

Farmer, J., J. Haslam, D. Day, T. Lian, C. Saw, P. Hailey, J. S. Choi, R. Rebak, N. Yang, R. Bayles, L. Aprigliano, J. Payer, J. Perepezko, K. Hildal, E. Lavermia, L. Ajdelsztajn, D. Branagan and B. Beardsley

30th Symposium on Scientific Basis for Nuclear Waste Management, D. Dunn, C. Poinssot and B. Begg, ed., **985**: 255-260 (2007).

The passive film stability of several Fe-based amorphous metal formulations have been found to be comparable to that of high-performance Ni-based alloys, and superior to that of stainless steels, based on electrochemical measurements of the passive film breakdown potential and general corrosion rates. Chromium (Cr), molybdenum (Mo) and tungsten (W) provide corrosion resistance; boron (B) enables glass formation; and rare earths such as yttrium (Y) lower critical cooling rate (CCR). The high boron content of this particular amorphous metal also makes it an effective neutron absorber, and suitable for criticality control applications, as discussed in companion publications. Corrosion data for SAM2X5 (Fe49.7Cr17.7Mn1.9Mo7.4W1.6B15.2C3.8Si2.4) is discussed here.

Impact Factor: N/A Cited Reference Count: 23

Topological feature extraction and tracking

Bremer, P. T., E. M. Bringa, M. A. Duchaineau, A. G. Gyulassy, D. Laney, A. Mascarenhas and V. Pascucci

30th Symposium on Scientific Discovery through Advanced Computing, ed., **78**: U76-U80 (2007).

Scientific datasets obtained by measurement or produced by computational simulations must be analyzed to understand the phenomenon under study. The analysis typically requires a mathematically sound definition of the features of interest and robust algorithms to identify these features, compute statistics about them, and often track them over time. Because scientific datasets often capture phenomena with multi-scale behavior, and almost always contain noise the definitions and algorithms must be designed with sufficient flexibility and care to allow multi-scale analysis and noise-removal. In this paper, we present some recent work on topological feature extraction and tracking with applications in molecular analysis, combustion simulation, and structural analysis of porous materials.

Impact Factor: N/A Cited Reference Count: 17

An expedited approach to evaluate the importance of different crystal growth parameters on laser damage performance in KDP and DKDP - art. no. 64031S

Negres, R. A., N. P. Zaitseva, P. DeMange and S. G. Demos

Annual Boulder Damage Conference on Laser Induced Damage in Optical Materials : 2006, G. J. Exarhos, A. H. Guenther and K. L. Lewis, ed., **6403**: S4031-S4031 (2007).

We investigate the laser-induced damage resistance at 355 nm in DKDP crystals grown with varying growth parameters, including temperature, speed of growth and impurity concentration. In order to perform this work, a DKDP crystal was grown over 34 days by the rapid-growth technique with varied growth conditions. By using the same crystal, we are able to isolate growth-related parameters affecting LID from raw material or other variations that are encountered when testing in different crystals. The objective is to find correlations of damage performance to growth conditions and reveal the key parameters for achieving DKDP material in which the number of damage initiating defects is minimized.

Impact Factor: N/A Cited Reference Count: 11

Thermal imaging investigation of modified fused silica at surface damage sites for understanding the underlying mechanisms of damage growth

Negres, R. A., M. W. Burke, P. DeMange, S. B. Sutton, M. D. Feit and S. G. Demos

Annual Boulder Damage Conference on Laser Induced Damage in Optical Materials 2006, G. J. Exarhos, A. H. Guenther and K. L. Lewis, ed., **6403**: 40306-40306 (2007).

We use an infrared thermal imaging system in combination with a fluorescence microscope to map the dynamics of the local surface temperature and fluorescence intensity under cw, UV excitation of laser-modified fused silica within a damage site. Based on a thermal diffusion model, we estimate the energy deposited via, linear absorption mechanisms and derive the linear absorption coefficient of the modified material. The results indicate that the damage growth mechanism is not entirely based on linear absorption. Specifically, the absorption cross-section derived above would prove insufficient to cause a significant increase in the temperature of the modified material under nanosecond, pulsed excitation (via linear absorption at ICF laser fluences). In addition, irreversible changes in the absorption cross-section following extended cw, UV laser exposure were observed.

Impact Factor: N/A Cited Reference Count: 8

Comparative study on the corrosion resistance of Fe-Based amorphous metal, borated stainless steel and Ni-Cr-Mo-Gd alloy

Lian, T., D. Day, P. Hailey, J. S. Choi and J. Farmer

30th Symposium on Scientific Basis for Nuclear Waste Management, D. Dunn, C. Poinssot and B. Begg, ed., **985**: 275-280 (2007).

Iron-based amorphous alloy FC49.7Cr17.7Mn1.9Mo7.4W1.6B15.2C3.8Si2.4 was compared to borated stainless steel and Ni-Cr-Mo-Gd alloy on their corrosion resistance in various high-concentration chloride solutions. The melt-spun ribbon of this iron-based amorphous alloy have demonstrated a better corrosion resistance than the bulk borated stainless steel and the bulk Ni-Cr-Mo-Gd alloy, in high-concentration chloride brines at temperatures 90 degrees C or higher.

Impact Factor: N/A Cited Reference Count: 5

Application of neutron-absorbing structural-amorphous metal (SAM) coatings for spent nuclear fuel (SNF) container to enhance criticality safety controls

Choi, J. S., C. Lee, J. Farmer, D. Day, M. Wall, C. Saw, M. Boussoufi, B. Liu, H. Egbert, D. Branagan and A. D'Amato

30th Symposium on Scientific Basis for Nuclear Waste Management, D. Dunn, C. Poinssot and B. Begg, ed., **985**: 249-254 (2007).

Spent nuclear fuel contains fissionable materials (U-235, Pu-239, Pu-241, etc.). To prevent nuclear criticality in spent fuel storage, transportation, and during disposal, neutron-absorbing materials (or neutron poisons, such as borated stainless steel, Boral (TM), Metamic (TM), Ni-Gd, and others) would have to be applied. The success in demonstrating that the High-Performance Corrosion-Resistant Material (HPCRM)([1]) can be thermally applied as coating onto base metal to provide for corrosion resistance for many naval applications raises the interest in applying the HPCRM to USDOE/OCRWM spent fuel management program. The fact that the HPCRM relies on the high content of boron to make the material amorphous - an essential property for corrosion resistance - and that the boron has to be homogenously distributed in the HPCRM qualify the material to be a neutron poison.

Impact Factor: N/A Cited Reference Count: 2

Overview of tabletop X-ray laser development at the Lawrence Livermore National Laboratory

Dunn, J., V. N. Shlyaptsev, J. Nilsen, R. F. Smith, R. Keenan, S. J. Moon, J. Filevich, J. Rocca, A. J. Nelson, J. R. Hunter, M. C. Marconi, Y. L. Li, A. L. Osterheld, R. Shepherd, H. Fiedorowicz, A. Bartnik, A. Y. Faenov, T. A. Pikuz, P. Zeitoun, S. Hubert, S. Jacquemot and M. Fajardo

X-Ray Lasers 2006, Proceedings, P. V. Nickles and K. A. Janulewicz. **115**: 1-11, 2007.

It is almost a decade since the first tabletop x-ray laser experiments were implemented at the Lawrence Livermore National Laboratory (LLNL). The decision to pursue the picosecond-driven schemes at LLNL was largely based around the early demonstration of the tabletop Ne-like Ti x-ray laser at the Max Born Institute (MBI) as well as the established robustness of collisional excitation schemes. These picosecond x-ray lasers have been a strong growth area for x-ray laser research. Rapid progress in source development and characterization has achieved ultrahigh peak brightness rivaling the previous activities on the larger facilities. Various picosecond soft-x-ray based applications have benefited from the increased repetition rates. We will describe the activities at LLNL in this area.

Impact Factor: N/A

The effect of laser pulse duration on laser-induced damage in KDP and SiO2

Carr, C. W., M. J. Matthews, J. D. Bude and M. L. Spaeth

Annual Boulder Damage Conference on Laser Induced Damage in Optical Materials: 2006, G. J. Exarhos, A. H. Guenther and K. L. Lewis, ed., **6403**: K4030-K4030 (2007).

We examine the effect of pulse duration on both density and morphology of laser-induced damage in KDP and SiO2. In both materials the density of damage sites scales with pulse duration to the similar to 0.4 power for 351-nm pulses between 1 and 10 ns. In SiO2 three types of damage sites are observed. The sizes of the largest of these sites as well as the size of KDP damage sites scale approximately linearly with pulse duration. Similarities of damage in very different materials points to properties of laser-induced damage which are material independent and give insight to the underlying physics of laser-induced damage.

Impact Factor: N/A

Patents

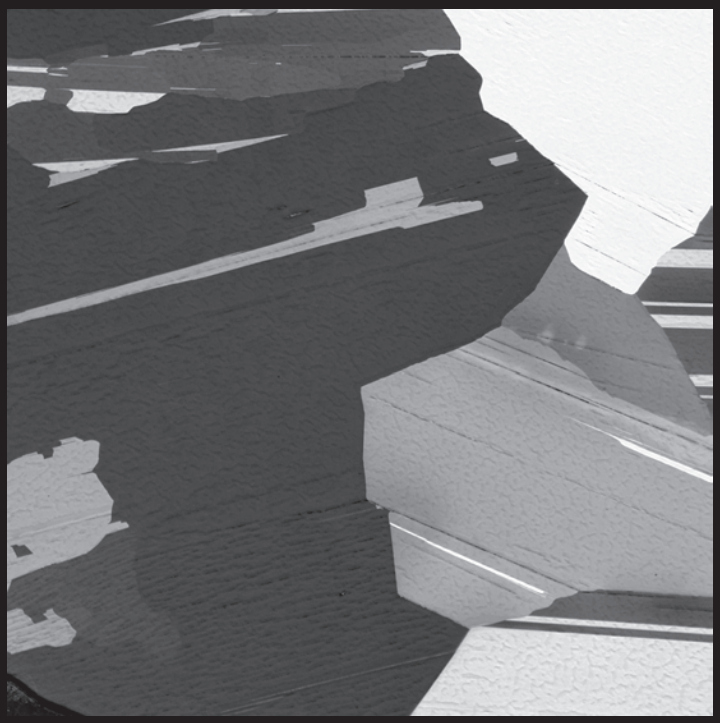

2007

Modified nitride fuel for compact and long-life reactors

Ebbinghaus, B., B. , J. S. Choi and T. Meier, C.

US Patent: WO2007011382A1, 2007.

A fuel element for a nuclear reactor comprises a modified nitride uranium or modified nitride plutonium fuel and additives that enhance properties of the modified nitride uranium or modified nitride plutonium fuel. In various embodiments nitride additives enhance compactness, long life, proliferation resistance, fuel safety, and waste management of the fuel element. In various embodiments the additives comprise at least one of zirconium nitride, thorium nitride, hafnium nitride, titanium nitride, or rare earth nitrides.

Diagnostic system for profiling micro-beams

Elmer, J. W., T. A. Palmer, A. T. Teruya and C. C. Walton

US Patent: US7288772B2, 2007.

An apparatus for characterization of a micro beam comprising a micro modified Faraday cup assembly including a first layer of material, a second layer of material operatively connected to the first layer of material, a third layer of material operatively connected to the second layer of material, and a fourth layer of material operatively connected to the third layer of material. The first layer of material comprises an electrical conducting material and has at least one first layer radial slit extending through the first layer. An electrical ground is connected to the first layer. The second layer of material comprises an insulating material and has at least one second layer radial slit corresponding to the first layer radial slit in the first layer of material. The second layer radial slit extends through the second layer. The third layer of material comprises a conducting material and has at least one third layer radial slit corresponding to the second layer radial slit in the second layer of material. The third layer radial slit extends through the third layer. The fourth layer of material comprises an electrical conducting material but does not have slits. An electrical measuring device is connected to the fourth layer. The micro modified Faraday cup assembly is positioned to be swept by the micro beam.

Indirect detection of radiation sources through direct detection of radiolysis products

Farmer, J. C., L. E. Fischer and T. E. Felter

US Patent: 2007.

A system for indirectly detecting a radiation source by directly detecting radiolytic products. The radiation source emits radiation and the radiation produces the radiolytic products. A fluid is positioned to receive the radiation from the radiation source. When the fluid is irradiated, radiolytic products are produced. By directly detecting the radiolytic products, the radiation source is detected.

Compositions of corrosion-resistant FE-based amorphous metals suitable for producing thermal spray coatings

Farmer, J. C., F. G. Wong, J. J. Haslam, X. Ji, S. D. Day, C. A. Blue, J. D. k. Rivard, L. F. Aprigliano, L. K. Kohler, R. Bayles, E. J. Lemieux, N. Yang, J. H. Perepezko, L. Kaufman, A. Heuer and E. Lavernia

US Patent: WO2007120205A2, 2007.

A method of coating a surface comprising providing a source of amorphous metal that contains manganese (1 to 3 atomic %), yttrium (0.1 to 10 atomic %), and silicon (0.3 to 3.1 atomic %) in the range of composition given in parentheses; and that contains the following elements in the specified range of composition given in parentheses: chromium (15 to 20 atomic %), molybdenum (2 to 15 atomic %), tungsten (1 to 3 atomic %), boron (5 to 16 atomic %), carbon (3 to 16 atomic %), and the balance iron; and applying said amorphous metal to the surface by a spray.

Fabrication of diamond shells

Hamza, A. V., J. Biener, C. Wild and E. Woerner

US Patent: 2007.

A novel method for fabricating diamond shells is introduced. The fabrication of such shells is a multi-step process, which involves diamond chemical vapor deposition on predetermined mandrels followed by polishing, microfabrication of holes, and removal of the mandrel by an etch process. The resultant shells of the present invention can be configured with a surface roughness at the nanometer level (e.g., on the order of down to about 10 nm RMS) on a mm length scale, and exhibit excellent hardness/strength, and good transparency in the both the infra-red and visible. Specifically, a novel process is disclosed herein, which allows coating of spherical substrates with optical-quality diamond films or nanocrystalline diamond films.

Modulated excitation fluorescence analysis

Weiss, S., A. Kapanidis, T. A. Laurence and N. K. Lee

US Patent: 2007.

Fluorescence, spectroscopy is used to analyze small numbers of molecules that are present in a relatively small detection volume or zone. Information regarding physical and chemical properties of these molecules is determined by rapidly modulating the wavelength, intensity and/or polarization of laser energy to excite fluorophores that are attached either to the molecule of interest or a molecule that interacts with the molecule of interest. The emission profile of the fluorophores is used to determine useful information about the labeled and/or non-labeled molecules including molecular interactions between the molecules.